Premixed flame inhibition by CF_3Br and $C_3H_2F_3Br$ (2-BTP)*

John L. Pagliaro[1, 2], N. Bouvet[2], Gregory T. Linteris[2]

[1]Dept. of Fire Protection Engineering; University of Maryland, College Park, MD 20742, USA

[2]Fire Research Division; National Institute of Standards and Technology; Gaithersburg, MD 20899, USA

To be submitted to *Combustion and Flame*

Key Words: Fire suppression; 2-BTP ($C_3H_2F_3Br$); Halon 1301 (CF_3Br); Burning velocity; Markstein length; refrigerant flammability.

Corresponding author:

John L. Pagliaro
National Institute of Standards and Technology
Engineering Laboratory
Gaithersburg, MD 20899
JohnLPagliaro@gmail.com
ph: 301-785-6182

Abstract

The un-stretched burning velocities and Markstein lengths of premixed CH_4- and C_3H_8-air flames with added $C_3H_2F_3Br$ (2-BTP) or CF_3Br (Halon 1301), have been studied experimentally and numerically. For CF_3Br flame inhibition, the un-stretched burning velocities, predicted using a recently updated kinetic model for CF_3Br flame inhibition, were in excellent agreement with the experimental results over a range of fuel-air equivalence ratio and CF_3Br loading. For $C_3H_2F_3Br$ flame inhibition, the un-stretched burning velocities predicted using a recently developed kinetic mechanism were in good agreement with the experimental results for most of the equivalence ratios tested; nonetheless, for very lean flames approaching the flammability limit, model predictions differed by up to 25 %, even for uninhibited flames. The influence of inhibitor on the flame response to stretch and susceptibility to instabilities was examined through consideration of the measured burned gas Markstein lengths. Markstein lengths were very large, leading to large stretch effects on the flame stability after ignition, and flame wrinkling during explosion tests, greatly increasing the rate of pressure rise. The influence of stretch with regard to flame inhibitor effectiveness is discussed.

1. **INTRODUCTION**

CF_3Br (Halon 1301) is an effective fire suppressant that has been largely phased out (by the Montreal Protocol) because of its high ozone depletion potential. Although a critical use exemption has been granted for use in commercial aircraft, the European Union is requiring replacement in new aircraft by 2018 and in existing aircraft by 2040. As a result of the expected phase-out, the Federal Aviation Administration (FAA) developed a minimum performance standard for the use of fire suppressants in cargo bays [1, 2] and tested three potential drop-in alternatives (C_2HF_5, $C_6F_{12}O$, and $C_3H_2F_3Br$). During the test (the Aerosol Can Test, FAA-ACT), a mixture of propane, ethanol, and water (simulating an exploding aerosol can) is impulsively released in the direction of a 15 kV DC arc that is 91.4 cm downstream of the release and near the center of a 11.4 m^3 chamber containing premixed ambient air and suppressant at specified concentrations. The test was designed to determine the minimum inerting concentration of a suppressant and to examine the consequences of adding sub-inerting concentrations. When sub-inerting concentrations of CF_3Br were added, the pressure rise was always lower than the pressure rise of the uninhibited case, whereas when sub-inerting concentrations of the proposed alternative $C_3H_2F_3Br$ (2-BTP) were added, the pressure rise was about three times larger than the uninhibited case (the pressure rise was about two times larger when adding sub-inerting concentrations of C_2HF_5 and $C_6F_{12}O$) [2, 3].

Recent work [4-6] performed equilibrium and perfectly-stirred reactor simulations with detailed chemistry to understand how CF_3Br, C_2HF_5, and $C_6F_{12}O$ impact the total heat release and reactivity in the FAA-ACT. Exothermic reaction of the alternative agents (C_2HF_5 and $C_6F_{12}O$) was found to add energy to the system, which not only increased the total heat release (and hence, the overpressure), but the reactivity as well (this was not the case with added CF_3Br). The analysis was later extended to include $C_3H_2F_3Br$ [7]; Burgess et al. [8] developed the first kinetic mechanism describing the decomposition of $C_3H_2F_3Br$ in hydrocarbon-air systems (down to C2 bromine-containing species). During parallel work [9], the CF_3Br mechanism reported in ref. [10] (which is used as a sub-mechanism to describe $C_3H_2F_3Br$ decomposition in the present work) was updated to include more accurate reaction rate data (Arrhenius coefficients) made available in literature since the original model was developed.

The objective of the present study is to provide experimental data for verification of the updated CF_3Br sub-model and the new $C_3H_2F_3Br$ sub-model, and to compare the inhibition performance of $C_3H_2F_3Br$ to CF_3Br for a wider range of premixed flame conditions and inhibitor concentrations than previously considered in ref. [11]. Laminar burning velocity is selected as a first step in model verification. Using high-speed shadowgraph images of spherically expanding flames, the burning velocity as a function of stretch is measured, from which the un-stretched laminar burning velocity and flame response to stretch (characterized by the Markstein length) are determined. Experiments are performed with CF_3Br and $C_3H_2F_3Br$ added to premixed CH_4- and C_3H_8-air flames, at ambient temperature and pressure (296 ± 2 K, 101 kPa), with initial equivalence ratios Φ of 0.6, 0.8, 1.0, and 1.2, and inhibitors added at volume fractions up to 3 % in the total reactant mixture. To test the kinetic mechanism, the flames are modeled as 1-D laminar flames using the Sandia PREMIX code and the predicted burning velocities are compared to the experimental values.

2. EXPERIMENTAL

2.1 Apparatus and procedure

The experiment developed for the present investigations (Fig. 1) is based on those of Faeth and coworkers [12-15] and Takizawa et al. [16]. A small spark-ignited spherically propagating flame develops in premixed gases contained in a larger chamber, and high-speed shadow graph images provide the flame speed. The spherical test chamber has an inner diameter of 380 mm, a volume of 30 L, and a wall thickness of 6.4 mm. The apparatus has vertical electrodes, an absolute pressure gauge, a dynamic pressure sensor, a thermocouple, and a mixing pump. Visual access is provided by two windows (102 mm in diameter and 25.4 mm thick) along the centerline of the chamber. The windows are polycarbonate (instead of quartz) to better resist the halogenated acids formed as product species in the present tests.

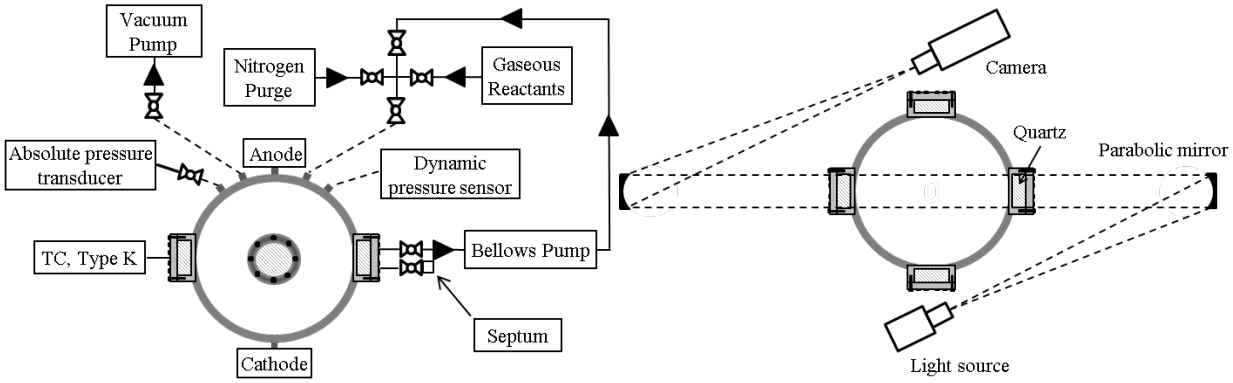

Fig. 1: Schematic diagram of the experiment (left) and shadowgraph setup (right).

The premixed reactants are prepared in the chamber via the method of partial pressures. First, a vacuum pump (Alcatel rotary vane) reduces the pressure below 100 Pa. Gaseous reactants are then added in order of lowest to highest concentration, with the partial pressure of each determined by an absolute pressure transducer (Omega PX409, which is periodically calibrated against a Baratron 627D pressure gage, claimed accuracy of 0.12 % of reading).

Liquid reactants (e.g., $C_3H_2F_3Br$) are injected into the chamber via a syringe and leak free septum (that is separated from the chamber by a ball valve that is closed prior to ignition). The desired mass is first obtained gravimetrically (using a Mettler PE 360 scale; 0.001g resolution), and after injection, the partial pressure is used for verification. A bellows pump (Parker Hannifin Model MB602XP) and external loop circulate the reactant gases for 3 min. (≈ 8 volume changes), after which the gases are allowed to settle for 10 min. The reactants are CH_4 (Matheson Tri-Gas, 99.97 % purity), C_3H_8 (Scott Specialty Gases, 99.0 % purity), CF_3Br (Great Lakes Chemical Corp., 99.6 % purity), and $C_3H_2F_3Br$ (American Pacific Corp., > 99 % purity). To provide the ambient air for the tests, in-house compressed air is filtered, dried, and conditioned with a 0.01 μm filter, a carbon filter, and a desiccant bed to remove small aerosols, organic vapors, and water vapor. The relative humidity of the air is less than 2 % for all tests according to measurements with a humidity gage (TSI Velocicalc 8386).

The reactant mixtures are centrally ignited with a capacitive discharge spark. Two vertical tungsten wire electrodes (0.8 mm diameter) form a 2 mm gap in the center of the chamber. A capacitive discharge system (similar to that of ref. [17]), consisting of a power supply (Acopian model PO15HP2, 1-15 kV) and a bank of interchangeable capacitors (1-100 nF), provides variable

ignition energies estimated to range from 0.05 mJ to 500 mJ. For most tests, the ignition energy is gradually increased until flame propagation occurs, ensuring the deposited energy is within an order of magnitude of the minimum value. For certain strongly-inhibited mixtures, higher ignition energies are required for the flame to propagate through the entire viewing window (because of the competing effects of stretch and the ignition energy [18], as described below).

The optical system for capturing the flame images is shown in Fig. 1. A z-type shadowgraph system, based on the recommendations of Settles [19], creates a shadow image of the flame, highlighting variations in the second derivative of the index of refraction. A 100 W mercury lamp creates a diverging beam that reflects off a parabolic mirror (f = 940 mm) creating a collimated beam that passes through the chamber. The beam then reflects off an identical parabolic mirror to a lens (Nikkor SLR, with a 135 mm focal length) attached to a high-speed camera (Phantom v7.0, operated at up to 7200 frames/s, monochrome images with a spatial resolution of 143 μm). Fig. 2 shows the recorded shadowgraph images of a stoichiometric CH_4-air flame with CF_3Br added at an agent volume fraction X_a=0.01.

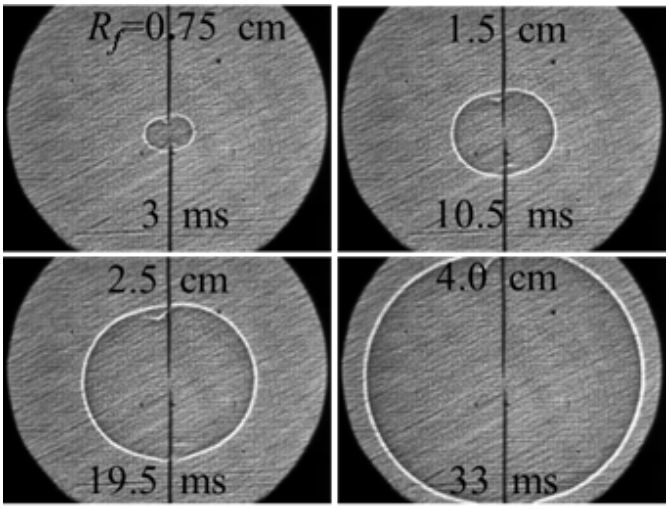

Fig. 2: Shadowgraph images of a propagating stoichiometric CH_4-air flame with 1 % CF_3Br.

In addition to visually recording flame propagation, a dynamic pressure sensor (PCB Piezotronics, 101A06; claimed accuracy of 0.1 % of reading) records the instantaneous pressure rise. After each test, the chamber is quickly vented and purged with nitrogen to reduce heat transfer from the product gases to the chamber. External fans cool the chamber to ambient temperature

(296 K ± 2 K) while it is purged with air, and then subjected to vacuum three times to ensure all products are removed before the next test.

2.2 Data reduction

The experiment provides an image of the flame as a function of time. Image analysis software (developed in-house) tracks the flame position (at the top, bottom, left, and right edge) as the location of the maximum positive gradient in light intensity when approaching the outer edge from the center (i.e. the hot gas boundary of the flame sheet [20]). For slow burning flames, which are of interest in this study, the influence of buoyancy is reduced by considering flame propagation in the horizontal direction only, as suggested in previous studies [16, 21-23]. The temporal evolution of the flame radius R_f yields the stretched flame speed, which is further processed to determine the burning velocity as a function of the stretch rate, as well as the un-stretched value (determined from extrapolations, as described below).

Following recommendations in the literature [23-30] , the range of flame radii included in data reduction is limited in order to accurately capture the relationship between burning velocity and stretch rate (the change in burning velocity as the radius changes can also be effected by confinement, radiation, ignition, instabilities, etc.). The upper bound R_{fU} is fixed at 3.5 cm for all tests, which is less than 25 % of the chamber radius as recommended in ref. [24] to avoid confinement effects. An R_{fU} smaller than 25% of the chamber radius was chosen to minimize the use of data affected by radiation [23, 25, 26], which occurs more so for slow burning flames with product gases of high emissivity (which are of interest in this study). For example, some of the flames described below have burning velocities near 4 cm/s, and produce high concentrations of HF and COF_2, which are strong radiators in the IR. Finally, larger flames can be more prone to have a cellular structure, which can greatly increase the burning velocity. By selecting an upper bound of 3.5 cm, all flame images post-processed to provide propagation rates were free from any cellularity.

The lower bound of flame radii (R_{fL}) to be included in data analysis excludes data potentially influenced by the ignition event or extreme nonlinearity during the early stages of flame propagation (the latter was shown to occur for mixtures with Lewis numbers significantly greater than unity and found to not be adequately captured by current extrapolation methods, leading to considerable errors in un-stretched results [26, 29]). Thus, R_{fL} ranges between 0.5 and 2.0 cm, and

is determined for each mixture by estimating (visually from a plot of R_f vs time, as in Fig. 3) R_f above which the curve is nearly linear. Fig. 3 illustrates two cases with varying degrees of non-linearity early on, for which an R_{fL} of 1.0 cm and 2.0 cm were selected. Note that in a select number of cases where high ignition energies (relative to our ignition capabilities) were required to generate sustained propagation, R_{fL} was set to 1.5 cm, a value slightly more conservative than those chosen in previous investigations (e.g. refs [26-29], with a 0.6 cm to 1.1 cm range).

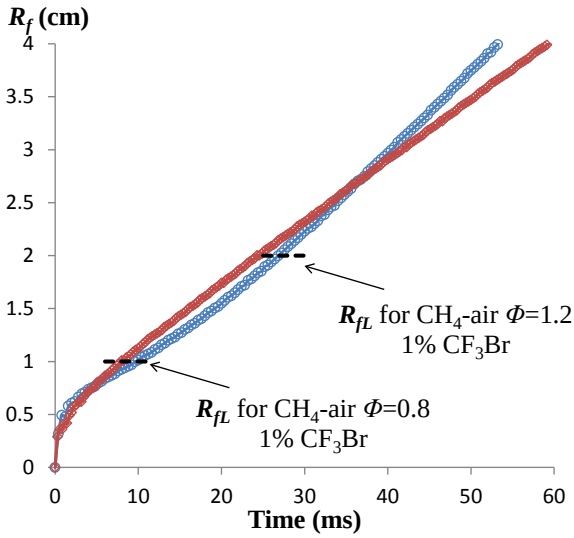

Fig. 3: Illustration of lower bound on flame radius used to eliminate non-linearity during the early stages of propagation.

For spherically symmetrical flame propagation, the flame speed in the laboratory frame of reference corresponds to the burned gas velocity S_b,

$$S_b = \mathrm{d}R_f/\mathrm{d}t \tag{1}$$

and is a function of the stretch rate, defined [31] as

$$\boldsymbol{K = \frac{1}{A_f}\frac{\mathrm{d}A_f}{\mathrm{d}t} = \frac{2}{R_f}\frac{\mathrm{d}R_f}{dt}} \tag{2}$$

where K is the stretch rate (s^{-1}), A_f is the flame surface area, and t is time. As seen in Eq. 2, the stretch rate decreases as the flame radius increases.

For kinetic model verification, the un-stretched burning velocity can be compared to the burning velocity predicted by numerical simulations of planar 1-D laminar flames. For this comparison, the measured burning velocities need to be extrapolated to un-stretched conditions (i.e., infinitely large flame radii), and various extrapolation procedures have been discussed in the

literature [30, 32-34]. In the present work, both linear and non-linear methodologies are considered.

Linear extrapolation

We use the linear relationship between burning velocity and stretch rate first employed by Markstein [35] and later expressed in the present form by Clavin [36],

$$S_b = S_b^o - L_b K \tag{3}$$

where S_b^0 is the un-stretched burned gas velocity and L_b is the burned gas Markstein length, which is a measure of the response of the flame to stretch. This functional form was derived for weakly stretched flames with near unity Lewis number *Le* (defined as the ratio of the mixture thermal diffusivity D_T to the mass diffusivity of the deficient reactant D_i). For the present inhibited mixtures, however, the controlling Lewis number is not obvious. Correlations exist for bi-component fuel mixtures [37], but a major assumption is that the two fuels independently react with the oxidizer and do not interact, which is not the case for the chemically active suppressants. For example, $C_3H_2F_3Br$ is both a fuel and oxidizer, and its decomposition products react with the fuel and its decomposition products, as well as oxygen; moreover, as noted by Babushok et al.[9], for CH_4-air flames inhibited by $C_3H_2F_3Br$, the fuel decomposition chemistry is intimately connected to the brominated species chemistry. Table 1 provides calculated *Le* values for lean (Φ = 0.8) and rich (Φ = 1.2) mixtures in CH_4-air or C_3H_8-air flames with $C_3H_2F_3Br$ added at a volume fraction of 2 % (assuming reactants are at 298 K). Clearly, significant departure from unity Lewis number is expected for the mixtures of interest (especially lean C_3H_8-air flames with added $C_3H_2F_3Br$), thus non-linear extrapolation is also performed as outlined below.

Table 1: Examples of fuel/agent/air mixture Lewis numbers at 2 % agent volume fraction. *Le* calculated as the ratio of the mixture thermal diffusivity (D_T) of the considered blend to the binary diffusion coefficient (D_i – reference species N_2) of either: i) the deficient species (either fuel or agent) for the lean cases, or ii) O_2 for the rich cases.

		Lean (Φ = 0.8)		*Rich (Φ = 1.2)*
Fuel	*Agent*	Le_{fuel}	Le_{agent}	Le_{O2}
CH_4	CF_3Br	0.93	1.70	1.00
	$C_3H_2F_3Br$	0.89	2.92	0.96
C_3H_8	CF_3Br	1.84	1.60	0.91

$C_3H_2F_3Br$	1.77	2.75	0.88

Non-linear extrapolation

Non-linear extrapolation is performed using the equations derived by Ronney and Sivashinsky [38] (for highly stretched flames with large *Le*), as formulated by Kelley et al. [39],

$$\left(\frac{S_b}{S_b^0}\right)^2 ln\left(\frac{S_b}{S_b^0}\right)^2 = -2\frac{L_b K}{S_b^0} - 2\frac{L_b}{S_b^0}\frac{dS_b}{dR_f} \tag{4}$$

Note that Eq. 4 is similar to the commonly used non-linear equation proposed in the earlier works of Kelley and Law [33],

$$\left(\frac{S_b}{S_b^0}\right)^2 \ln\left(\frac{S_b}{S_b^0}\right)^2 = -2\frac{L_b K}{S_b^0} \tag{5}$$

It should be noted that while the non-linear methods generally provide more accurate results compared to the linear one, Wu et al. [34] recently showed that none of the existing extrapolation methods capture the true non-linear relationship between flame speed and stretch rate when *Le* is considerably lower than unity ($L_b < 0$).

In applying Eq. 4 for data reduction, an expanded form, suggested in ref. [39]

$$\frac{S_b}{S_b^0}\left[1 + \frac{2L_b}{R_f} + \frac{4{L_b}^2}{{R_f}^2} + \frac{16{L_b}^3}{3{R_f}^3} + o^4\left(\frac{L_b}{R_f}\right)\right] = 1 \tag{6}$$

is applied because it is more numerically stable. Finally, using integrated forms of Eqs. 3 and 6 (as in [39-41]) reduces uncertainty resulting from the numerical differentiation required to solve Eqs. 3 and 6. Thus, the equations used to reduce the raw data and extract the un-stretched burning velocity S_b^0 and Markstein length L_b become

$$R_f = S_b^0 t - 2L_b \ln R_f + c_1 \tag{7}$$

$$S_b^0 t + c_2 = R_f + 2L_b \ln R_f - 4\frac{L_b^2}{R_f^2} - \frac{8}{3}\frac{L_b^3}{R_f^3} \tag{8}$$

where the variables c_1 and c_2 are integration constants. The variables S_b^0, L_b, c_1, and c_2 are determined using a non-linear least squares optimization routine that fits Eqs. 7 and 8 to the experimentally measured flame radius versus time $R_f(t)$. From conservation of mass across the flame sheet, the un-stretched unburned gas velocity S_u^0 is then obtained:

$$S_u^0 = \frac{\rho_b}{\rho_u} S_b^0 \quad (9)$$

where ρ_u and ρ_b are the unburned and burned gas densities. The burned gas is assumed to be in chemical equilibrium and ρ_b is taken from a constant-pressure, constant-enthalpy calculation at the initial temperature and pressure of each test using the CEA2 routine of Gordon and McBride [41]. Thermodynamic data for these calculations are from the NASA database [42] (included in CEA2), the NIST (National Institute of Standards and Technology) HFC mechanism [43], and the $C_3H_2F_3Br$ mechanism [8] (the latter two sources are described in more detail below).

Tests are performed at 296 K ± 2 K and 1.01 bar and are repeated twice for each mixture. For each test, the extrapolation equations are fit to the R_f vs. t data from the left and right side flame tracking locations. The fitting parameters (S_b^0, L_b, and c) from the two sides are then averaged. Lastly, the results of the multiple tests are averaged to produce the burning velocities and burned gas Markstein lengths reported in the present study, which have standard deviations that are generally around 0.3 cm/s and 0.15 mm, with maximum values of 0.9 cm/s and 0.7 mm. Fig. 4 shows the average S_b from the left and right tracking locations of select CF_3Br-inhibited C_3H_8-air tests (symbols) as a function of stretch rate, along with the linear extrapolation to zero-stretch conditions (dotted lines). For clarity, data with Markstein lengths greater than, less than, and nearly equal to unity are labeled. Note that elsewhere in the present paper, the reported values of S_u^0 and L_b are from the non-linear fit of R_f vs. t, as mentioned above. In Fig. 4, dR_f/dt (i.e., S_b) are extrapolated to S_b^0 using the linear and non-linear methods (Eqs. 3 and 4) strictly for illustrating the extrapolation to zero-stretch conditions and the differences in the flame response to stretch, characterized by L_b. As the figure shows, for these conditions there is no discernable difference in the value of un-stretched burning velocity from using either the linear or non-linear extrapolation methods.

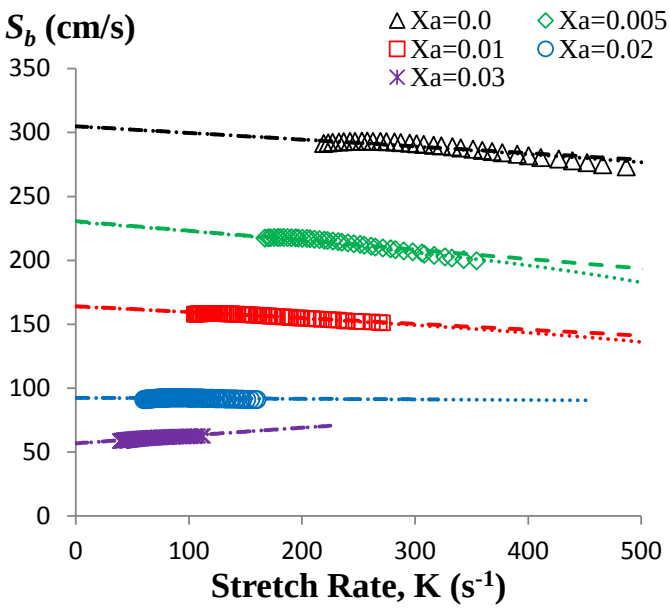

Fig. 4: Burned gas velocity versus stretch rate for CF_3Br-inhibited C_3H_8-air mixtures at Φ=1.2. The symbols are the experimental data, the dashed lines are the linear extrapolation (Eq. 3), and the dotted lines are the non-linear extrapolation (Eq. 4) to zero-stretch conditions.

2.5 Uncertainties and measurement accuracy

The uncertainties in experimental burning velocity are reported as expanded uncertainties $U = ku_c$ determined from a combined standard uncertainty u_c and a coverage factor $k = 2$ corresponding to a level of confidence of 95 %. The combined standard uncertainty is determined using the root-sum-of-squares (RSS) method of combining individual uncertainty components, as outlined in ref. [44]. As described by Chen [26], uncertainties in the initial conditions can be propagated to uncertainties in the burning velocities. Using his estimations based on numerical modeling, uncertainties in the initial temperature, pressure, mixture equivalence ratio, and inhibitor concentration, of 3 K, 1.3 kPa, 1 %, and 0.3 % result in a maximum expanded relative uncertainty of 13 % in S_u^0, which occurs at lean conditions when the uncertainty in the equivalence ratio has the largest effect on the reported data.

Measurement uncertainty is not the only cause of inaccuracy in the reported data. Buoyancy, radiation, and non-linear stretch effects can cause the measured result to differ from the speed of the ideal 1-D planar adiabatic flame or even the true speed of a spherically propagating flame (this is particularly important when comparing experimental data to numerical predictions). Higher inaccuracy exists for slow burning flames most affected by buoyancy and radiation. In addition, higher uncertainty is expected for mixtures with Lewis numbers far from unity (i.e. *Le*

<< 1 and *Le* >> 1) because, for highly non-equidiffusive mixtures, the extrapolation methods fail to fully capture the non-linearity between the burning velocity and stretch rate, as demonstrated in ref.[34]. While these factors cannot be eliminated in the present study, their influence was minimized by using only the portion of the R_f vs. t data described above.

3. NUMERICAL METHODS

Equilibrium product species and their thermodynamic state are calculated for a constant-pressure, constant-enthalpy process using the EQUIL subroutine [45] (reactants at 298.15 K and 1.01 bar). Planar adiabatic freely propagating premixed flame structures are calculated using the Sandia PREMIX code [46-48]. The mass, species, and energy conservation equations are solved for each reactant mixture at an initial temperature and pressure of 298.15 K and 1.01 bar, with air modeled as N_2 and O_2 at volume fractions of 0.79 and 0.21. The Soret effect is considered and molecular diffusion is modeled using the mixture-averaged formulation. Large computational domains are used with final gradient (GRAD) and curvature (CURV) parameters set to 0.05. As such, the number of grid points ranged from 310 to 420, with the final adjustment of the GRAD and CURV parameters adding about 100 grid points, and yielding a burning velocity change of less than 2 % (the change was typically much less and decreased as the burning velocity increased).

A comprehensive reaction mechanism previously assembled in ref. [9], and included here as supplementary material, is used to model CH_4- and C_3H_8-air flames with added CF_3Br or $C_3H_2F_3Br$. The complete mechanism is composed of several sub-mechanisms. Hydrocarbon-air reactions are modeled with the C1-C4 mechanism of Wang et al. [49]. C1-C3 hydrofluorocarbon reactions are modeled with an updated version of the NIST HFC mechanism [43, 50], with the updates summarized in refs. [5, 9]. Decomposition reactions of brominated C1 species in the presence of hydrocarbon-air are modeled with an updated version of the original CF_3Br mechanism of Babushok et al. [10], as described in ref.[9]. Lastly, reactions involving the larger brominated species of $C_3H_2F_3Br$ decomposition have been developed by Burgess et al. [9]. It should be emphasized that the mechanism assembled for the present verification study is considered only as a starting point. Numerous changes to both the rates and the reactions included may be made once additional experimental and theoretical data become available (this is particularly true for the new $C_3H_2F_3Br$ decomposition sub-mechanism).

4. RESULTS AND DISCUSSION

4.1 Experimental validation

To validate the accuracy of the present experimental system and data reduction methods, the un-stretched, unburned gas burning velocity S_u^0 of CH_4- and C_3H_8-air flames over a range of fuel-air equivalence ratios are presented and compared with other data in the literature. (In these comparisons and others, the non-linear extrapolation method was used to reduce the present data, unless otherwise stated). Fig. 5 compares the present CH_4-air ($0.6 \leq \Phi \leq 1.3$) measurements to spherically propagating flame [28, 51-53] and counterflow flame [54, 55] datasets, as well as numerical predictions using the Wang mechanism [56]. For each experimental dataset, the inclusion of an (L) or (NL) in the figure legend specifies whether linear or non-linear extrapolation was performed. Burning velocities are in excellent agreement with the previous results and agree well with predictions, except for $\Phi \leq 0.8$, where measured S_u^0 is 10 % to 25 % lower. For $\Phi \geq 0.9$, measured S_u^0 is within 3 % of the predictions. At lean conditions, previously determined experimental burning velocities are in general lower than the predictions, with the exception of refs. [53, 55]. The agreement between the present data and previously published data show that the new experiment provides accurate burning velocity measurements for CH_4-air mixtures.

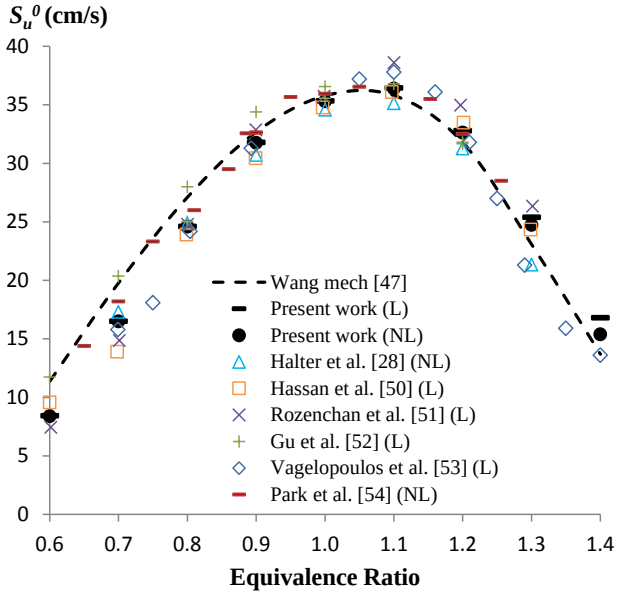

Fig. 5: Burning velocity of premixed CH_4-air flames at 298 K and 101 kPa as a function of equivalence ratio, together with previously published results (symbols) and 1-D planar adiabatic simulation (dashed line).

Fig. 6 compares burning velocities for C_3H_8-air flames against spherically propagating [15, 56], counterflow [54, 57], and heat flux-stabilized [58] flame datasets, along with numerical predictions with the Wang mechanism [49]. As in Fig. 5, the use of linear or non-linear extrapolation is specified for each dataset by an (L) or (NL). At lean conditions, the present S_u^0 results are in excellent agreement with the previous experiments and with the numerical predictions. For rich conditions ($\Phi > 1.0$), the present data are on the lower end of the experimental scatter, but exhibit reasonable agreement with the model predictions.

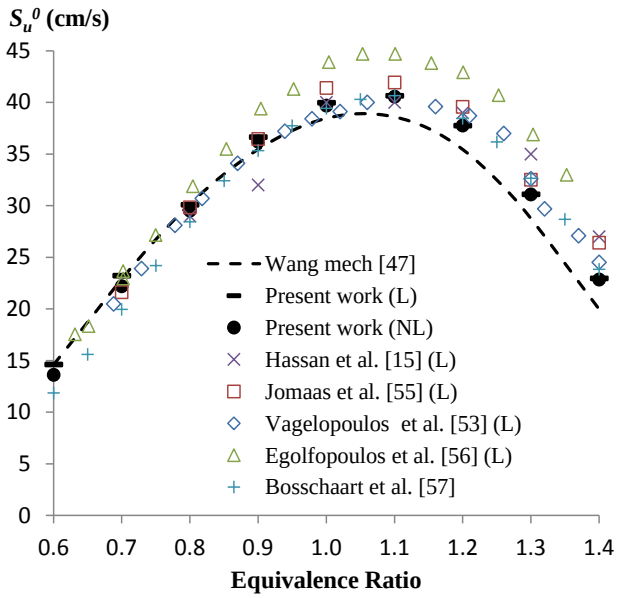

Fig. 6: Burning velocity of premixed C_3H_8-air flames at 298 K and 101 kPa as a function of equivalence ratio, together with previously published results (symbols) and 1-D planar adiabatic simulation (dashed line).

We further validate the experimental results by comparing burned gas Markstein lengths L_b for CH_4-air flames to results in the literature. Fig. 7 presents the linearly (left frame) and non-linearly (right frame) extracted results according to Eq. 7 and Eq. 8, along with previous experimental [28, 51-53, 59] and computational [27] datasets. Similar to what was seen in the above S_u^0 comparison, the present L_b values fall within the scatter of previously published data for the entire range of equivalence ratio. Non-linearly extracted L_b values are in excellent agreement with the results of refs. [28, 59] and linearly extracted L_b values are closest to the results of ref. [28]. Moreover, at lean conditions, the L_b values obtained by the linear and non-linear method are similar, whereas at rich conditions the linear method yields L_b values that are considerably larger. The larger scatter in linearly-extracted Markstein lengths (compared to non-linearly extracted

ones) has been demonstrated [26] to be the result of higher sensitivity to the lower and upper radius bounds considered during extrapolation.

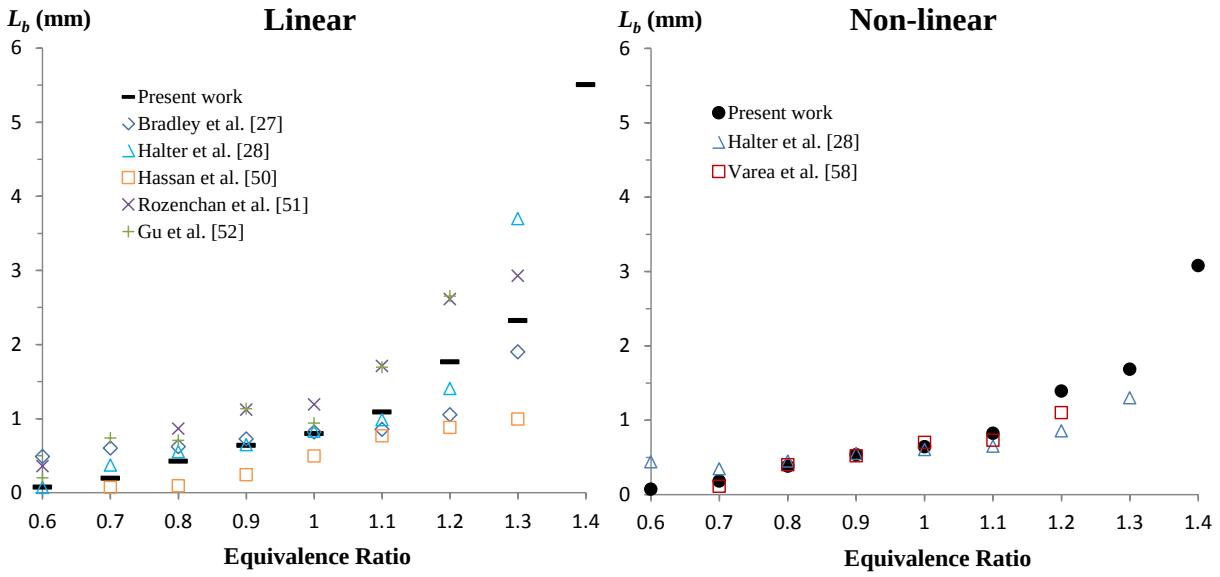

Fig. 7: Burned gas Markstein lengths of premixed CH_4-air flames as a function of equivalence ratio, together with previously published results. Linear method: left frame; non-linear method: right frame.

Fig. 8 provides Markstein lengths L_b of C_3H_8-air flames as a function of equivalence ratio. The present linearly and non-linearly extrapolated experimental data are plotted together (because fewer data are available in the literature) and compared to previous spherically expanding experimental [60-62] and numerical [63] data (linear and non-linear extrapolations are noted by the dashed and circle symbols respectively). For rich conditions, present and previously reported Markstein lengths are all in good agreement regardless of the extrapolation method. At leaner conditions, the scatter becomes larger, with the linearly extracted Markstein lengths generally higher. As observed for the CH_4-air flames, the present non-linear L_b values are in excellent agreement with the non-linear data reported by Varea [62].

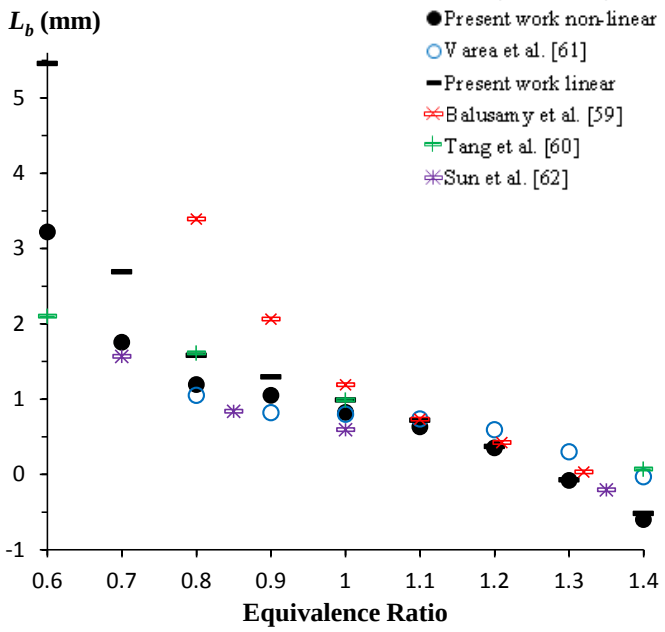

Fig. 8: Burned gas Markstein lengths of premixed C_3H_8-air flames as a function of equivalence ratio, together with previously published results.

4.2 Influence of CF_3Br and $C_3H_2F_3Br$ on S_u^0

Fig. 9 presents the burning velocities (bottom curves in each frame) for premixed CH_4-air (left frames) and C_3H_8-air (right frames) flames with added CF_3Br (triangles) or $C_3H_2F_3Br$ (circles), for S_u^0 determined using the non-linear extrapolation method. Computed equilibrium adiabatic flame temperatures are shown by the lines without symbols for CF_3Br and $C_3H_2F_3Br$. The upper, middle, and lower frames provide data for equivalence ratios of 1.2, 1.0 and 0.8 (based on the uninhibited mixture prior to agent addition).

Rich cases (Φ = 1.2)

As shown in Fig. 9, $C_3H_2F_3Br$ provides a larger reduction in both S_u^0 and T_{ad} as compared to CF_3Br (top left frame). At X_a = 0.02, the computed T_{ad} for the $C_3H_2F_3Br$-inhibited mixture is 147 K lower than for the CF_3Br case and both agents are found to prevent ignition[1]. Similar results are seen when adding the agents to the rich C_3H_8-air flames (top right frame). For instance, $C_3H_2F_3Br$ lowers the burning velocity 38 % and 56 % more than CF_3Br at X_a = 0.01 and 0.02. For the same conditions, the reduction in T_{ad} is 74 K and 142 K larger with $C_3H_2F_3Br$. At X_a = 0.03,

[1] The phrase "prevent ignition" and term "non-ignition" are used throughout to identify conditions where a flame was either not observed or did not propagate throughout the entire viewing window when applying the maximum available ignition energy. We avoid "extinction" and "limits" because the concentrations for which non-ignition occurs are both vessel specific and based on the available ignition energy range in the present study. We do not claim the concentrations causing non-ignition to be representative of flammability or ignition limits.

non-ignition occurs with $C_3H_2F_3Br$, whereas flame propagation was observed for the CF_3Br case with S_u^0 = 6.8 cm/s.

Stoichiometric cases

For the stoichiometric CH_4-air mixture (middle left frame), CF_3Br and $C_3H_2F_3Br$ provide similar reductions in burning velocity. While the flame adiabatic temperatures are similar for X_a < 0.01, the decrease of T_{ad} is larger with $C_3H_2F_3Br$ addition when X_a > 0.01. For example, at X_a = 0.03 T_{ad} is 170 K lower with $C_3H_2F_3Br$ than with CF_3Br, and both agents prevent ignition. Similar trends are again observed when adding agents to C_3H_8-air flames (middle right frame), although for C_3H_8–air flames, $C_3H_2F_3Br$ seems more efficient at reducing S_u^0 at higher agent loadings (X_a > 0.02).

Lean cases (Φ = 0.8)

At lean conditions, CF_3Br provides a larger reduction in the burning velocity (as compared to richer cases) at all agent concentrations considered. For example, for Φ = 0.8, addition of 2 % CF_3Br is found to prevent ignition of both CH_4-air and C_3H_8-air flames (bottom frames), whereas addition of 3 % $C_3H_2F_3Br$ still allows stable flames, with corresponding burning velocities of 5.8 cm/s and 8.7 cm/s. Note that for CF_3Br addition to the lean flames, T_{ad} decreases mildly with X_a increase, as it was for the case for the rich and stoichiometric flames. In contrast, the addition of $C_3H_2F_3Br$ to either CH_4- or C_3H_8-air flames increases the adiabatic flame temperature, by up to 200 K at X_a = 0.018, and then the increase is reduced as X_a increases.

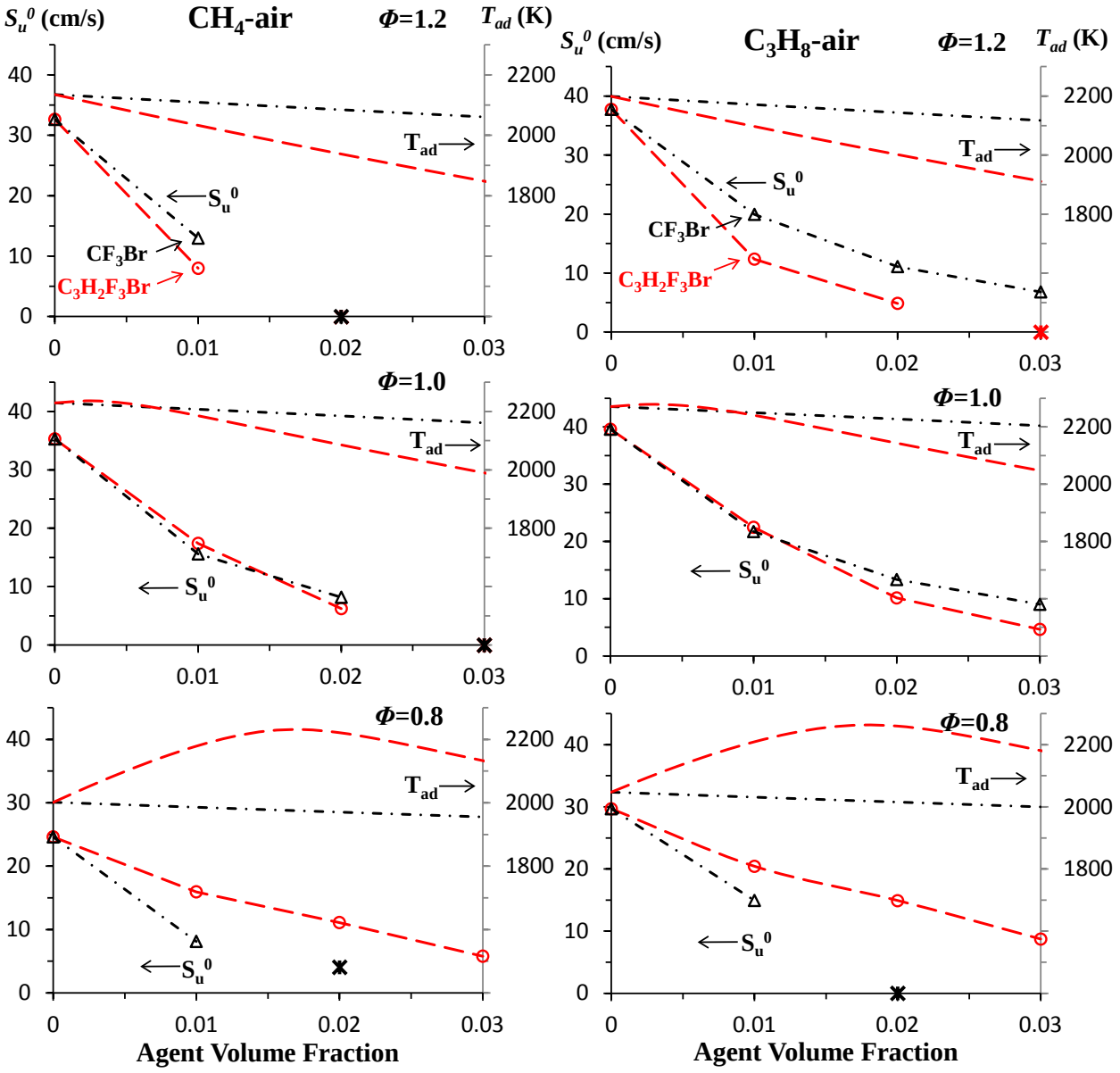

Fig. 9: Laminar burning velocity S_u^0 and adiabatic flame temperature T_{ad} of CH_4-air (left) and C_3H_8-air (right) with added CF_3Br and $C_3H_2F_3Br$. For clarity, lines connect the experimental data points (and do not represent predictions). Data at the highest value of X_a and S_u^0=0 represent points of unsuccessful flame propagation or non-ignition.

The differences in the behavior of added CF_3Br and $C_3H_2F_3Br$ to lean and rich flames is worthy of discussion. It has been shown [64, 65] that the chemical inhibition by halogen-containing agents results from reduction of active flame radical (H, OH, O) concentrations by halogenated intermediates, which lowers the overall flame reactivity. Since the atomic concentrations of fluorine and bromine are identical for CF_3Br or $C_3H_2F_3Br$ addition (at the same X_a), the mechanisms of reduction in the chain-carrying radical concentrations due to radical

trapping and radical recombination cycles are not expected to differ significantly. Rather, the change in the effective stoichiometry due to the fuel component (C_xH_y-) of the $C_3H_2F_3Br$ (as compared to CF_3Br) is likely the cause.

To illustrate the effect of $C_3H_2F_3Br$ on the overall stoichiometry, an overall equivalence ratio $\Phi_{overall}$ can be defined that incorporates the agent fuel effect. The balance equation for the fuel/agent/air system can be written as:

$$\rho C_a H_b + \alpha C_c H_d F_e Br_f + \gamma[0.21O_2 + 0.79N_2] = \beta CO_2 + \lambda HF + \mu H_2O + \delta Br + \eta N_2$$

Note that when fluorine is present, the main combustion products are dependent on the ratio of hydrogen to fluorine atoms ([F]/[H]). For the present inhibited mixtures, [F]/[H] is always less than unity, so that only the fluorinated product HF need be considered (unlike cases with [F]/[H] > 1, for which CFO_2 and CF_4 formation must be considered). The stoichiometric proportion of air γ_{stoic} is found by performing balances on C, H, F, Br, and O atoms:

$$\gamma_{stoic} = \rho(a + b/4) + \alpha(c + d/4 - e/4)$$

so that $\Phi_{overall}$ is expressed as:

$$\Phi_{overall} = [(\rho + \alpha)/(\gamma_{actual})]/[(\rho + \alpha)/(\gamma_{stoic})]$$

Fig. 10 shows the change in $\Phi_{overall}$ with agent addition ($C_3H_2F_3Br$ or CF_3Br) to C_3H_8-air at initial equivalence ratios of 0.8, 1.0 and 1.2. When CF_3Br is added, there is minimal change in the overall equivalence ratio. Conversely, as $C_3H_2F_3Br$ is added, the overall equivalence ratio is shifted considerably toward rich conditions. For instance, the initially lean C_3H_8-air flame at Φ = 0.8 reaches stoichiometry when $C_3H_2F_3Br$ is added at $X_a \approx 0.015$. The results observed in Fig. 10 are consistent with the relative inhibitor efficiencies observed in Fig. 9. For the lean flame, the peak temperature with added $C_3H_2F_3Br$ occurs near the concentration corresponding to $\Phi_{overall} = 1$ ($X_a \approx 0.018$). At lean conditions, CF_3Br has a lesser impact on T_{ad} and $\Phi_{overall}$ (compared to $C_3H_2F_3Br$) and reduces burning velocity more effectively. At rich conditions, the higher inhibition efficiency of $C_3H_2F_3Br$ is likely the result of the larger shift in $\Phi_{overall}$ toward even richer conditions.

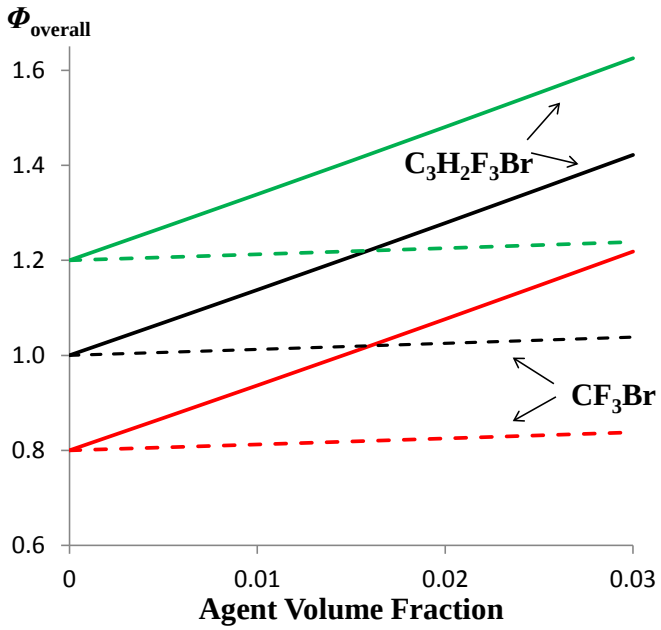

Fig. 10: Overall equivalence ratio as $C_3H_2F_3Br$ (dashed lines) or CF_3Br (solid lines) is added to C_3H_8-air flames at different initial equivalence ratios.

The stoichiometry of the flame affects the radical trapping by fluorinated intermediates (e.g., CF_3, CF_2, etc.) and catalytic radical recombination by Br-species. For example, Fig. 11 shows the peak (solid lines) and equilibrium (dashed lines) OH volume fraction as a function of the volume fraction of added $C_3H_2F_3Br$ or CF_3Br, for Φ=0.53, 1.0, and 1.33. (Note that the response for OH is approximately the average of the response for O and H, so that the net radical behavior is approximated by that of OH.) The first thing to note is that the equilibrium OH volume fraction is strongly affected by addition of $C_3H_2F_3Br$, but minimally by CF_3Br. For example, with addition of $C_3H_2F_3Br$, the equilibrium OH volume fraction is increased (non-monotonically) by a factor of 21 for lean flames (at X_a,=0.03) but reduced by a factor of about 9 and 11 for stoichiometric and rich flames (at X_a,=0.02, and more at higher X_a). For CF_3Br addition, the equilibrium OH volume fraction decreases monotonically about the same amount (36 % to 60 % reduction at X_a,=0.02) for the lean and stoichiometric flames, respectively. The behavior of the peak OH volume fraction is also different for the two agents: CF_3Br always drives the OH towards equilibrium (i.e., the catalytic radical recombination effect), and the catalytic efficiency is lower for richer flames (i.e., higher agent loadings are required for the peak OH volume fraction to reaches the equilibrium value for richer flames). The agent $C_3H_2F_3Br$ also drives the OH to equilibrium relatively efficiently for the lean flame, but poorly (i.e., little catalytic effect) for the initially stoichiometric

and rich flames. That is, with $C_3H_2F_3Br$ addition, most of the radical reduction in the stoichiometric and rich flames occurs due to reduction in the equilibrium value. Moreover, for the lean flame, the equilibrium value increases rapidly with $C_3H_2F_3Br$ addition (due to the increase in peak flame temperature), so that catalytic radical recombination cycle, while working, does not help reduce burning velocity. Thus, $C_3H_2F_3Br$ is a more effective agent than CF_3Br for rich and stoichiometric flames because it reduces the equilibrium radical concentrations more so than does CF_3Br.

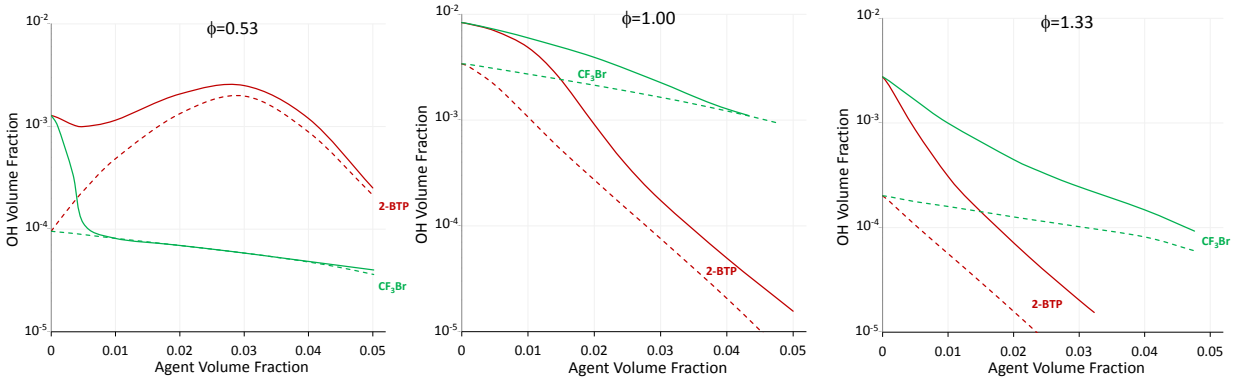

Fig. 12: Overall equivalence ratio as $C_3H_2F_3Br$ (dashed lines) or CF_3Br (solid lines) is added to C_3H_8-air flames at different initial equivalence ratios.

4.3 CF_3Br model verification

As a check of the updated C1 brominated-species sub-mechanism, the experimentally measured burning velocities are compared to numerical predictions of CF_3Br-inhibited flames. Fig. 13 presents experimental values of S_u^0 (symbols) together with numerical predictions (lines), for flames of CH_4-air (left frame) and C_3H_8-air (right frame). The separate curves shows results at a given value of the initial, uninhibited, equivalence ratio Φ = 0.6, 0.8, 1.0, and 1.2. The open symbols denote values of S_u^0 determined using non-linear extrapolation (described above) while the bars (-) show values obtained using linear extrapolation. As indicated, for nearly all data collected (except the two circled conditions), the difference between the two extrapolation methods is very small. The agreement between the predicted and measured values of S_u^0 is also very good, typically within about 7 %, which is much less than the estimated maximum uncertainty in S_u^0 (± 13 %). Moreover, the present burning velocities agree well with previously reported values for CF_3Br-inhibited stoichiometric CH_4-air flames [11, 66, 67], as illustrated in Fig. 14. For C_3H_8-air flames (right frame in Fig. 13), the agreement between measured and predicted S_u^0 is similar to

that observed for the inhibited CH_4-air flames: numerical predictions slightly over-predict inhibition, but by less than 8 % for most conditions, with the exception of Φ = 1.0 and X_a = 0.03 where the model over-predicts inhibition by 18 %. When adding CF_3Br to CH_4- and C_3H_8-air flames, the marginal reduction in S_u^0 decreases as the agent concentration increases in both experiments and predictions, as has been discussed previously [68, 69]. Although no burning velocity data could be collected for inhibited flames at very lean conditions (Φ = 0.6), numerical predictions are provided to illustrate the expected inhibition. For both the CH_4-air and C_3H_8-air flames at Φ = 0.6, non-ignition occurred at the lowest concentration tested (X_a = 0.005).

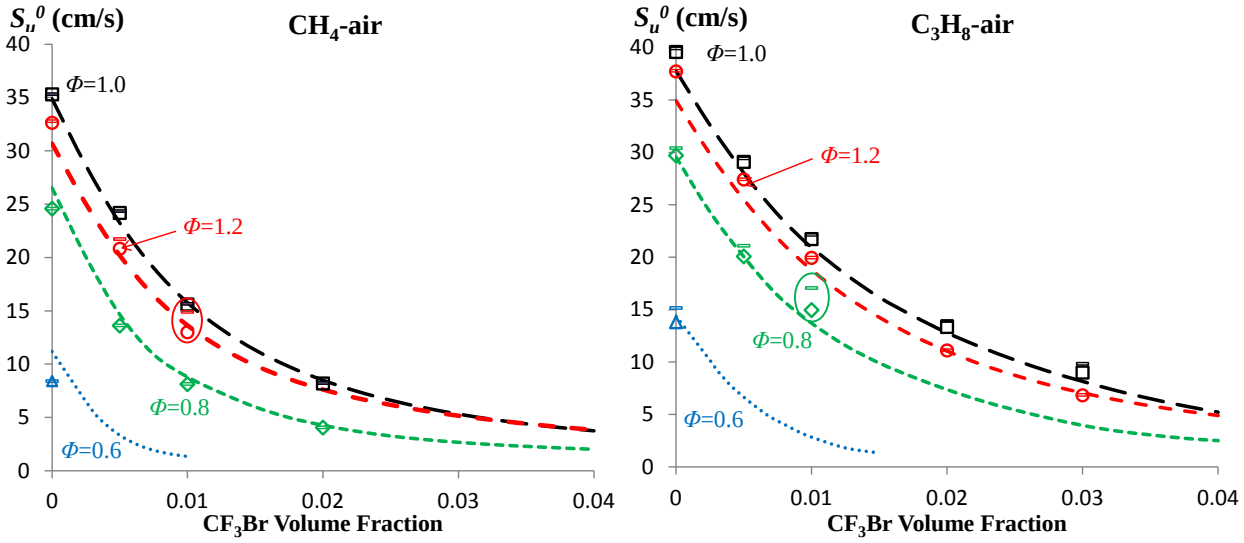

Fig. 13: Comparison of experimental (symbols) and numerical (lines) S_u^0 for CF_3Br-inhibited CH_4-air (left frame) and C_3H_8-air (right frame) at Φ = 0.6, 0.8, 1.0, and 1.2; open symbols are non-linearly extracted and bars are linearly extracted.

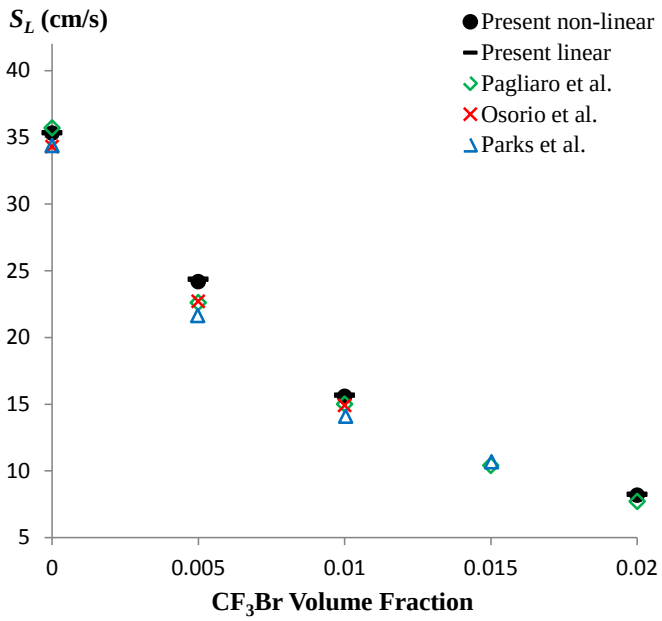

Fig. 14: Burning velocity of stoichiometric CH_4-air with added CF_3Br, together with previously published results.

Recently, Osorio et al. [67] compared measured burning velocities of CF_3Br-inhibited CH_4- and C_3H_8-air flames with numerical predictions. A constant-pressure spherically expanding flame experiment provided burning velocity as a function of stretch, which was extrapolated to zero-stretch conditions using the linear method described above. These values of extracted S_u^0 were then compared with predictions of the 1-D planar laminar burning velocity from the Sandia PREMIX code, using the NUI-Galway mechanism (to describe hydrocarbon decomposition) [70] and the CF_3Br mechanism of ref. [10]. With CF_3Br added at X_a = 0.005 or 0.01 and ($0.8 \leq \Phi \leq 1.2$), the burning velocity predictions were found to be consistently higher than the experimental values. It was unclear whether the discrepancy was the result of inaccuracies in the original CF_3Br model [10] or bias associated with the linear method for extrapolating the burning velocity to un-stretched conditions (as described by other researchers [28, 32, 33]). Thus, to explore the source of the discrepancies, tests were repeated for the conditions of their experiments, and the data were reduced using the present linear and non-linear extrapolation methods. Finally, the values of S_u^0 were predicted using PREMIX simulations using the present kinetic model.

The results from ref. [67] are compared to the present results in Fig. 15. Burning velocities as a function of equivalence ratio are shown for flames of CH_4-air (left frame) and C_3H_8-air (right frame) with CF_3Br volume fractions of 0, 0.005 and 0.01. The solid lines, solid bars, and solid

circles show the present predictions, linearly extrapolated data, and non-linearly extrapolated data. The dashed lines and open bars show the predictions and linearly extrapolated data from ref. [67]. As seen in the figure, the present experimental data are very close to each other when using either linear or non-linear extrapolations (except for the cases of rich CH_4-air and lean C_3H_8-air flames with CF_3Br volume fraction of 0.01). The present experimental data are also close to the experimental data of Osorio, generally within 7 % and with a maximum difference of 20 %. As seen in Fig. 15, burning velocity measurements from both studies are much closer to the present predictions using the updated CF_3Br mechanism proposed in ref [9] (as opposed to the older mechanism used by Osorio et al.). Overall, the predictions of ref. [67] are 4 % to 28 % and 13 % to 35 % higher than the present non-linearly extracted S_u^0, while the present predictions fall within ±9 % of the non-linearly extracted values. Although the underlying hydrocarbon mechanisms are different, it appears that the updates[2] outlined in ref. [9] have significantly improved the accuracy of the CF_3Br model.

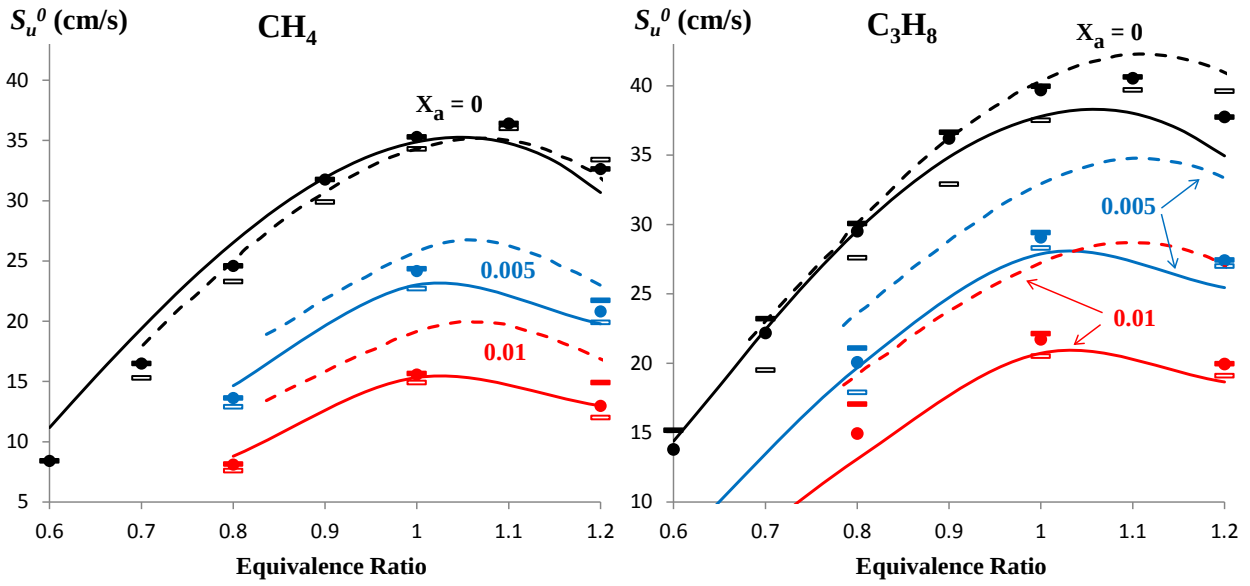

Fig. 15: Comparison of present measured and predicted S_u^0 with those of Osorio et al. [67] for CH_4-air (left) and C_3H_8-air (right) flames with added CF_3Br. Solid bars and circles represent the present linearly and non-linearly extracted S_u^0; solid lines represent the present predictions; open bars and dashed lines are the linearly extracted and predicted S_u^0 from ref. [67].

[2] The improved performance of the updated model is the result of the inclusion of more accurate kinetic rate data made available in the literature since the original model was developed (and not based on the present measurements and predictions). As summarized in ref. [9], Arrhenius rate coefficient data was updated for 1/3 of the 100 reactions contained in the model.

4.4 $C_3H_2F_3Br$ model verification

To validate the new $C_3H_2F_3Br$ (2-BTP) kinetic model, measured S_u^0 for CH_4- and C_3H_8-air flames with added $C_3H_2F_3Br$ are compared to predictions. For each fuel-air mixture, four different initial equivalence ratios are considered (Φ = 0.6, 0.8, 1.0, and 1.2). Fig. 16 presents the the present experimental S_u^0 (symbols) together with the numerical predictions (lines) for flames of CH_4-air (left frame) and C_3H_8-air (right frame). The open symbols and bars denote values of S_u^0 determined using the non-linear and linear extrapolation methods, and as seen for the CF_3Br-inhibited flames, nearly all the data (except for the circled condition) have very similar results using the two methods (well within the experimental uncertainty). In addition, burning velocities of $C_3H_2F_3Br$-inhibited CH_4-air flames (left frame) determined from the *constant-volume* spherically expanding method [11] (note that these data are not stretch corrected, but instead, extrapolated from experimental data at large flame radii when the stretch rate is small) are shown for Φ=1.0 and 0.6 (X symbols). The experimental data from the two methods agree within about 12 % and 7 % for Φ=1.0 and Φ=0.6.

For $C_3H_2F_3Br$ added to CH_4-air, the model predictions are within 9 % of the experimental results for Φ = 1.0 and 1.2, while for Φ = 0.8, the inhibition performance is over-predicted in the range at low agent concentrations, with measured S_u^0 higher than predictions by up to 18 % (the discrepancy increases as X_a increases). At Φ=0.6, the model over-predicts inhibition performance by 25 % (which is close to the measurement accuracy of ≈ 2 cm/s), but captures the non-monotonic behavior as the $C_3H_2F_3Br$ concentration increases; the flame speed initially drops up to X_a = 0.01, before it increasing for $0.01 \leq X_a \leq 0.03$, and finally decreases as more $C_3H_2F_3Br$ is added. Previous work with the BTP model [9] showed that the drop in S_u^0 at low concentrations, followed by the rise at higher concentrations, was the result of the competition between radical scavenging by the halogenated species (Br and F participate in chain terminating reactions) and the additional heat release associated with the decomposition of $C_3H_2F_3Br$ in the lean CH_4-air environment.

For $C_3H_2F_3Br$ added to C_3H_8-air, burning velocity predictions are within 7 % of the experimental results for the stoichiometric and rich flames, with the exception of the prediction for Φ = 1.2 and X_a = 0.02 which is higher by 22 % (but still within the measurement uncertainty of ≈ 2 cm/s). The model predictions are once again higher than the experimental values at the lean

conditions; at Φ = 0.8, prediction accuracy decreases as X_a increases, the relative error in S_u^0 at X_a = 0.03 being about 25 %.

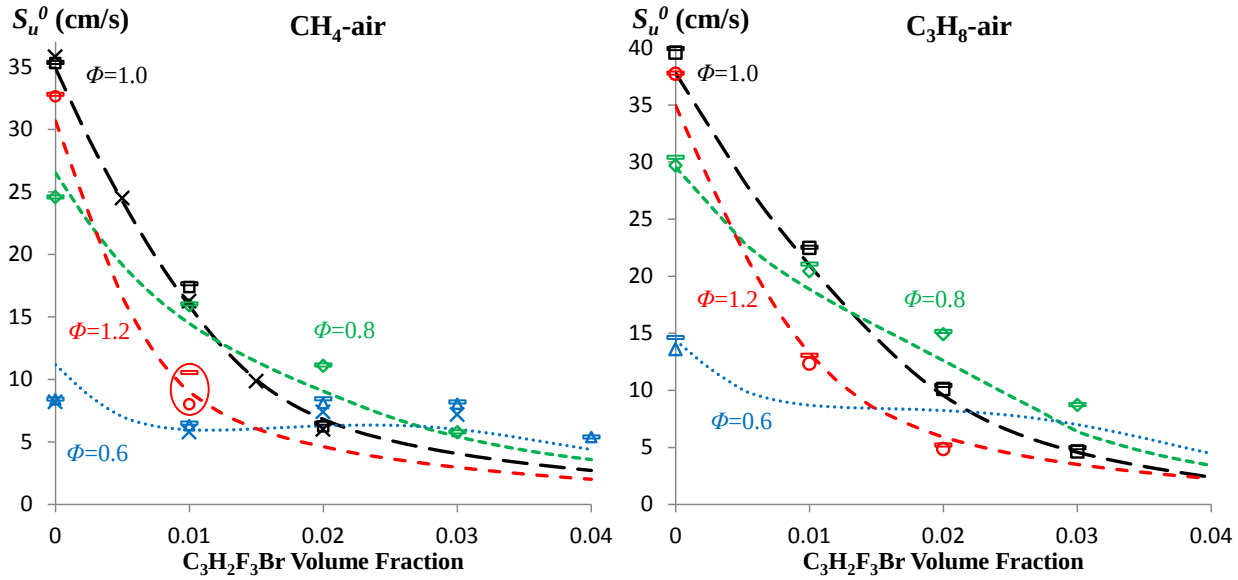

Fig. 16: Comparison of experimental (symbols) and numerical (lines) S_u^0 for $C_3H_2F_3Br$-inhibited CH_4-air (left) and C_3H_8-air (right) flames at Φ = 0.6, 0.8, 1.0, and 1.2; open symbols are non-linearly extracted, bars are linearly extracted, and crosses are from ref. [11].

4.5 Sensitivity analysis

Normalized sensitivity coefficients in the form of logarithmic derivatives ($\delta \ln S_u / \delta \ln A_i$) are determined from the PREMIX simulations for CH_4-air flames with added CF_3Br and $C_3H_2F_3Br$ to identify the brominated reactions that burning velocity is most sensitive to. In Fig. 17, the brominated reactions with the highest absolute sensitivities are shown for stoichiometric CH_4-air flames with CF_3Br (grey bars) and $C_3H_2F_3Br$ (black bars) added at X_a = 0.03 (a positive normalized sensitivity coefficient indicates that an increase in the Arrhenius pre-exponential factor A increases S_u^0, and vice versa). Burning velocities are found to be sensitive to numerous brominated reactions participating in both the recombination of H_2 and the generation of HBr. In general, the CF_3Br inhibited flame is more sensitive to the brominated reactions in Fig. 17, with higher sensitivity to the top three reactions because the concentrations of hydrocarbon fragments that serve as alternative paths for HBr and BR_2 formation are lower than in the $C_3H_2F_3Br$ inhibited flame. In regard to the updates made to the CF3Br mechanism in ref. [9], reactions 6-9 in Fig. 17 are among the reactions for which more accurate rate coefficients were assigned.

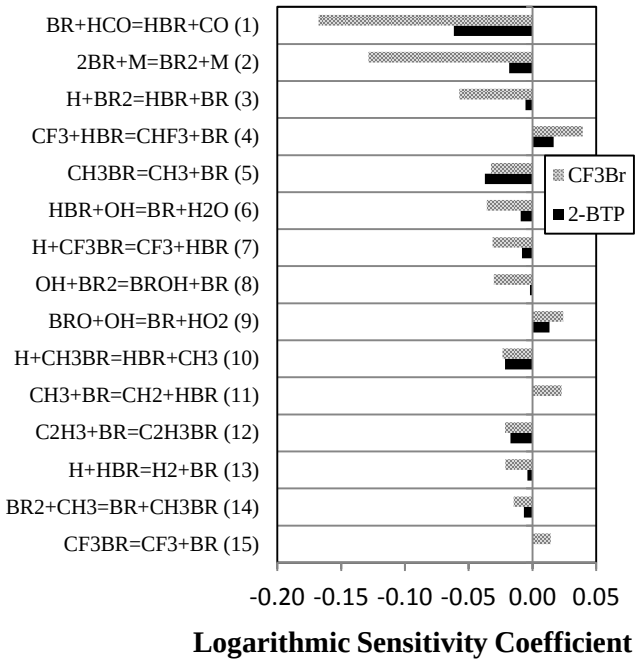

Fig. 17: Sensitivity coefficients for stoichiometric CH_4-air flames with CF_3Br and $C_3H_2F_3Br$ added at a volume fraction of 3%.

4.6 Flame stability and S_u^0

Referring back to Fig. 13, flames with higher predicted values of S_u^0 sometimes propagated less well than flames with lower values. For certain mixtures, applying near-minimum ignition energies established a flame that extinguished soon after. When this occurred, the experiment was repeated with a higher energy until the flame successfully propagated through the entire viewing window. For other tests, such as CH_4-air at Φ = 1.2 with 2 % CF_3Br, the maximum available ignition energy initiated reaction, but did not produce sustained propagation. Hence, as shown for hydrocarbons [72], non-ignition of mixtures with added CF_3Br or $C_3H_2F_3Br$ is not entirely controlled by S_u^0, but instead, dependent on other factors (i.e., in the present study non-ignition occurred over a range of predicted S_u^0, depending on the initial equivalence ratio). For example, flame propagation was observed for lean CH_4-air (Φ = 0.8) with 2 % CF_3Br and not for rich CH_4-air (Φ = 1.2) with 2 % CF_3Br although the predicted planar burning velocities were 4.3 cm/s and 6.6 cm/s, respectively. In other words, the mixture with the lower predicted burning velocity successfully propagated through the viewing window and the mixture with the higher predicted burning velocity did not. With added $C_3H_2F_3Br$, successful flame propagation could not be obtained for lean C_3H_8-air (Φ=0.6) although it could for Φ = 1.0, X_a = 0.03 and Φ = 1.2, X_a = 0.02, for which S_u^0 which had burning velocities lower by ~ 2 cm/s.

Similar observations were made by Qiao et al. [23] when measuring burning velocities of CH_4-air flames diluted with chemically passive suppressants (N_2, Ar, CO_2, and He). During their study, successful flame propagation was observed for stoichiometric CH_4-air flames diluted with N_2, Ar, and CO_2 with predicted S_u^0 around 5 cm/s. On the contrary, flame propagation was not observed for a He-diluted flame, even though the predicted S_u^0 was around 10 cm/s. For certain mixtures, the change in the response to stretch may cause stretch-induced quenching during the early stages of flame growth, as observed in ref. [23]. To interpret the influence of inhibitors on the flame response to stretch, Markstein lengths are examined in the following section.

4.7 Influence of agents on Markstein length and minimum ignition energy

Flame propagation speed and stability depend upon the flame's response to stretch (which can be characterized by the Markstein length L_b) as well as the stretch condition of the particular configuration [73]. As described above, by considering flames of different radii, the present experiment provides the laminar burning velocity as a function of the stretch rate (from which the Markstein length L_b can be determined, using either the linear or non-linear analysis of the data). For example, Fig. 18 shows the non-linearly extracted burned gas Markstein lengths L_b for CH_4-air flames (left frames) and C_3H_8-air flames (right frames) as a function of the volume fraction of added CF_3Br (top) and $C_3H_2F_3Br$ (bottom). The different symbols (with lines connecting the data) show results at different Φ. As frequently reported in literature, the Markstein lengths of uninhibited CH_4-air and C_3H_8-air increase and decrease respectively as the equivalence ratio increases. (Opposite trends exist because the diffusivity of CH_4/C_3H_8 is higher/lower than the diffusivity of air [73].)

For CF_3Br addition, Fig. 18 shows that the influence on the flame response to stretch is not only dependent on the initial equivalence ratio and fuel type, but also on the volume fraction of added CF_3Br. For rich flames of CH_4, L_b increases as the concentration of CF_3Br increases, while for lean flames, the opposite is true (L_b becomes more negative) and for stoichiometric flames, L_b is small, becomes slightly more positive up to X_a = 0.005, above which the effect is relatively neutral. For C_3H_8-air flames, the trends are generally opposite (L_b for lean flames becomes more positive with added CF_3Br, etc.), although the influence is stronger and L_b becomes more positive for stoichiometric flames as well. For the rich flames (Φ = 1.2), L_b first increases slightly then decreases and becomes negative. With added CF_3Br, the Markstein lengths are similar in

magnitude to the Markstein lengths for extremely rich ($\Phi \approx 7$) H_2-air flames [74], highlighting the strong sensitivity of the inhibited flame speeds to the stretch rate.

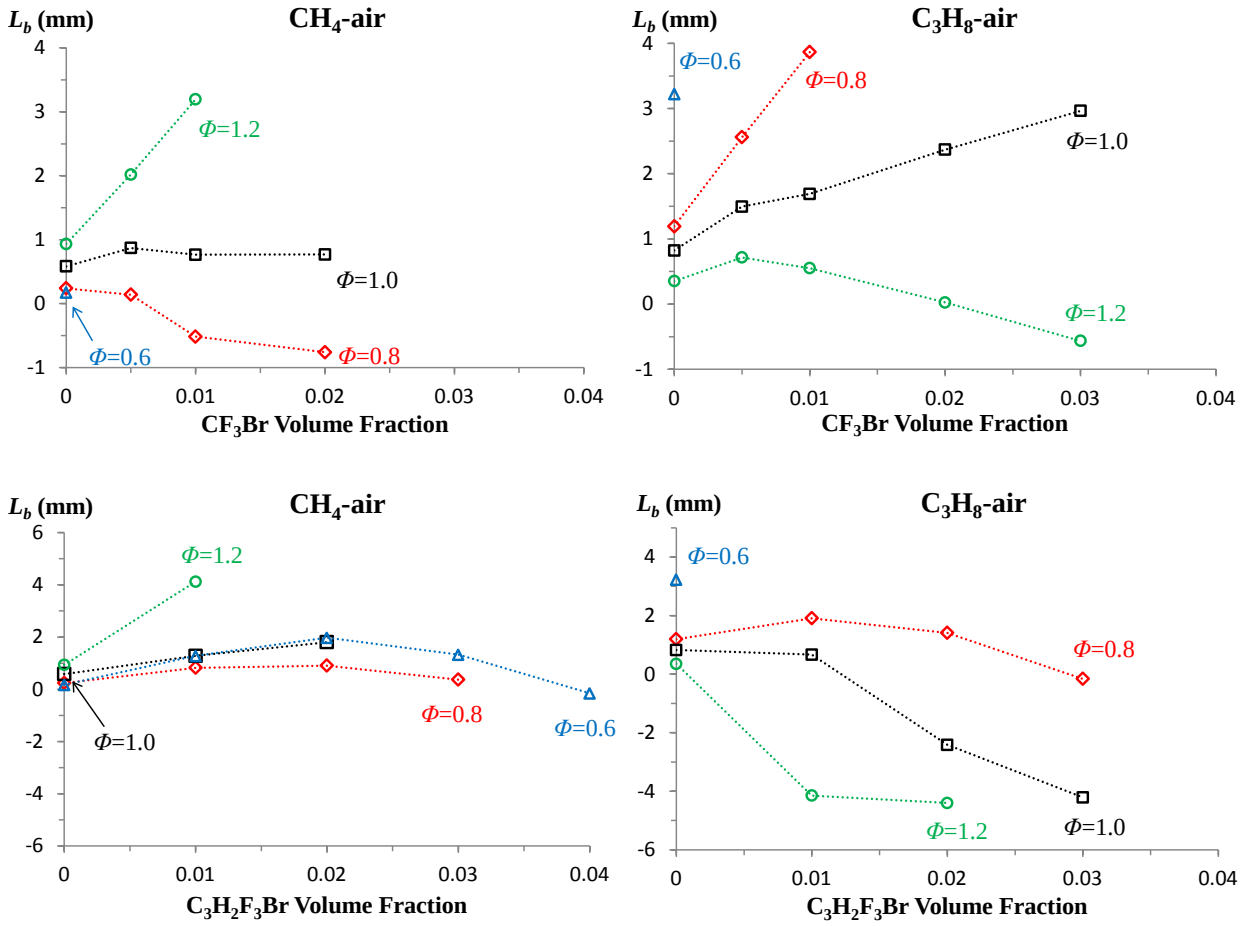

Fig. 18: Burned gas Markstein lengths for CH_4-air (right frames) and C_3H_8-air (left frames) with added CF_3Br (top) and $C_3H_2F_3Br$ (bottom). For clarity, lines connect the experimental data points and do not represent predictions.

For $C_3H_2F_3Br$ addition, (bottom frames of Fig. 18), the Markstein length is affected somewhat differently than with CF_3Br. In general, for $C_3H_2F_3Br$ addition relative to CF_3Br addition, all of the curves in Fig. 18 are pushed down (for either CH_4- or C_3H_8-air flames); i.e. L_b increases less or decreases more with agent addition. Non-monotonic behavior for the L_b, such as that shown in Fig. 18 for lean CH_4– and C_3H_8-air flames with added $C_3H_2F_3Br$, has also been observed for CH_4-air flames with added H_2 [75-77]; it was attributed to changes in the both the mixture Lewis number and overall activation energy as the concentration of H_2 increased [76].

The influence of inhibitors on the sensitivity of the flame response to stretch (as characterized by the Markstein length) can explain the non-ignition of some flames with higher values of the planar, un-stretched burning velocity S_u^0 than certain flames that successfully propagated. For spherically expanding flames with positive burned gas Markstein lengths, the burning velocity increases toward the planer 1-D burning velocity as the stretch rate decreases (i.e. as the flame radius increases). Hence, when L_b is positive the flame propagation is slowest at small flame radii, and as L_b gets larger, a critical flame radius must be reached for sustained propagation to occur [18, 78]. As detailed in the previous section, a well-established flame can form early on and then quickly extinguish because the supplied ignition energy is not sufficient to drive the flame to the critical radius. For example in Fig. 13, for the case of rich CH_4-air (Φ = 1.2) with added CF_3Br at X_a = 0.02, partial flame propagation was observed (when applying the maximum available ignition energy). For this mixture, a flame propagated roughly 1.5 cm before extinction occurred. Apparently, the critical radius for these mixtures is larger than 1.5 cm, which is about a factor of 3 larger the critical radius determined for rich H_2-air flames (Φ = 5.1 and P = 101 kPa) in ref. [18]. The same behavior was observed for lean (Φ = 0.8) C_3H_8-air flames with added CF_3Br at X_a = 0.02. Both of these apparent anomalies can be explained by considering the effect of CF_3Br on L_b. As seen in Fig. 18 for the rich CH_4-air and lean C_3H_8-air flames with added CF_3Br, L_b increases sharply as the concentration of CF_3Br increases; hence, the large positive value of L_b makes the flames propagate faster at large radii. Excessive spark energy aids the flame propagation at small radii which is why initial flame propagation is observed; as the radius grows, the propagation speed increases, so that there is a critical flame radius required for the flame to self-propagate once the excess ignition energy is depleted.

4.8 Influence of agents on Markstein length and flame stability

The burned gas Markstein length not only shows how the propagation speed changes with the stretch rate, it is also a measure of the susceptibility of a flame to diffusional-thermal instability (i.e., flame transition to cellular structure) [73]. Kim et al. [79] added CF_3Br to H_2-air flames at equivalence ratios Φ = 0.8, 1.0, and 1.8 and found that the flame stability decreased as the inhibitor concentration increased regardless of the fuel-air ratio, causing the flames to wrinkle and promoting transition from laminar to turbulent propagation. As the wrinkles grow, the surface area of the flame sheet increases which increases the mass burning rate. Thus, the reduced stability resulting from agent addition is undesirable and offsets the reduction in the mass burning rate that

occurs through chemical inhibition [79]. Currently, no data are available on how chemically active suppressants influence the stability of hydrocarbon-air flames, especially with added $C_3H_2F_3Br$.

If agent addition changes the Markstein length from positive to negative (or more negative) it makes the flame unstable and susceptible to flame wrinkling (a positive L_b signifies a stable flame and vice versa). Referring to Fig. 18, adding CF_3Br or $C_3H_2F_3Br$ can increase or decrease flame stability depending on the fuel, the initial equivalence ratio, and the agent concentration. CF_3Br addition promotes flame wrinkling for lean CH_4-air flames and rich C_3H_8-air flames; $C_3H_2F_3Br$ addition has lesser effect for CH_4-air flames, but more strongly promotes wrinkling for rich C_3H_8-flames (or stoichiometric flames above $X_a = 0.005$). Thus, in contrast to what was observed in ref. [79] for H_2-air flames, the Markstein length, and hence flame stability, is not *always* reduced when inhibitor is added to hydrocarbon-air flames.

When an inhibitor significantly reduces flame stability ($L_b << 0$), laminar burning velocity may not be the only metric for ranking suppression effectiveness. The sign of L_b suggests the expected flame dynamics for conditions beyond the small radii flames used to determine burning velocity in the present study. To illustrate this, the rate of pressure rise versus time (left frame) and the flame propagation speed versus stretch rate (right frame) are shown in Fig. 19 for rich ($\Phi = 1.2$) C_3H_8-air flames with 1 % $C_3H_2F_3Br$ or 2 % CF_3Br. (Note that the stretched burning velocity data is extracted when the flame radii is small and the pressure is constant. The rate of pressure rise is extracted from the latter part of each test as the flame continues to propagate through the remaining chamber volume.) These mixtures (properties listed in Table 2) were chosen because they have similar un-stretched laminar burning velocities of 12.3 cm/s and 11.1 cm/s and similar adiabatic flame temperatures of 2002 K and 2144 K, but different Markstein lengths; the $C_3H_2F_3Br$-inhibited flame ($L_b = – 4.15$ mm) is more unstable than the CF_3Br-inhibited flame ($L_b = 0.03$ mm). As seen in Fig. 19 (left frame), even though the burning velocities are similar (differing only by 1.2 cm/s), the peak rate of pressure rise dP/dt_{max} is more than double for the $C_3H_2F_3Br$-inhibited mixture (164.7 bar/s compared to 73.4 bar/s), and the time of the onset of cellularity (determined from the video images, and illustrated in the figure by the black stars) occurs much earlier. Thus, the influence of the inhibitor on flame stability and response to stretch (described by the Markstein length) is significant and may influence the behavior of the suppressants in tests such as the FAA-ACT. Moreover, flammable mixtures containing new low-GWP refrigerants,

which are in many ways similar to the present hydrocarbon flames with added suppressant, may exhibit similar trends to those observed in the present work.

Table 2: Adiabatic flame temperature, un-stretched burning velocity, Markstein length, and peak rate of pressure rise for a rich C_3H_8-air flame inhibited by 1 % $C_3H_2F_3Br$ and 2 % CF_3Br.

C_3H_8-air Φ=1.2		
Agent	$C_3H_2F_3Br$	CF_3Br
X_a	0.01	0.02
T_{ad} (K)	2002	2144
S_u^0 (cm/s)	12.34	11.11
L_b (mm)	-4.15	0.03
dP/dt_{max} (bar/s)	164.7	73.4

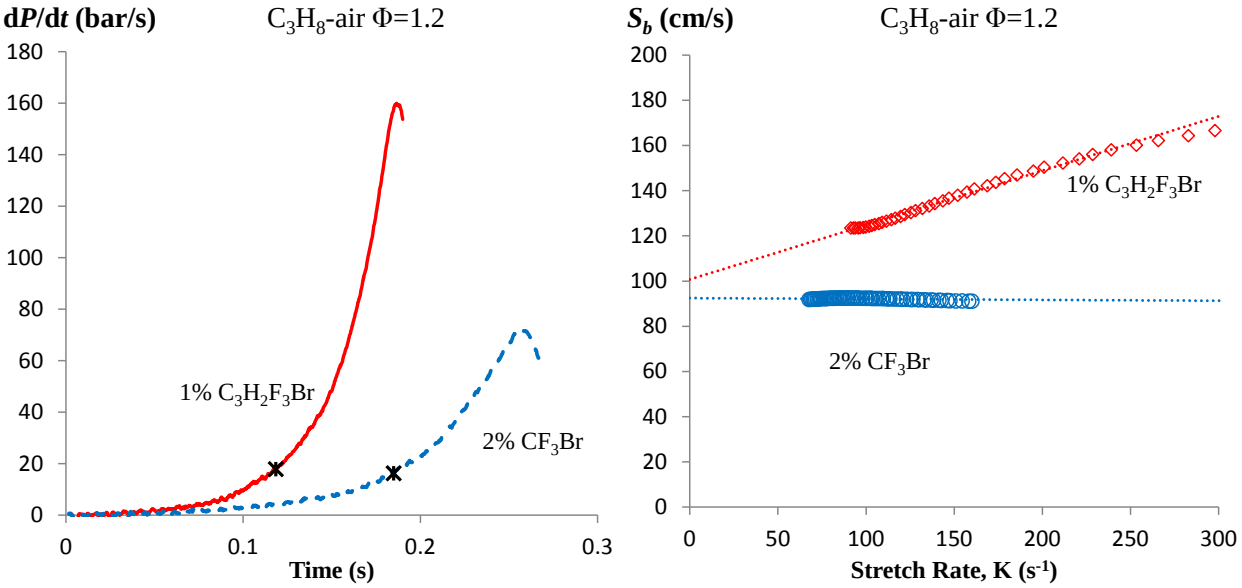

Fig. 19: Rate of pressure rise versus time for combustion of rich C_3H_8-air (Φ=1.2) with 1 % $C_3H_2F_3Br$ or 2 % CF_3Br added (the two mixtures have similar S_u^0 and T_{ad}). The stars mark the instance when cellular flame structures were first observed in the videos.

5. CONCLUSIONS

Unexpected overpressures occurred in the FAA Aerosol Can Test when the fire suppressant $C_3H_2F_3Br$ (2-BTP) was added. To aid in interpretation, previous researchers developed a kinetic model for inhibition by $C_3H_2F_3Br$ and updated the model for CF_3Br. As a first step in model verification, burning velocity measurements and numerical simulations with detailed chemistry

were performed for CH_4-air and C_3H_8-air flames inhibited by these compounds. Comparison of the inhibited flame burning velocities highlighted differences in performance and the conditions for which each agent was most effective.

Experimentally measured spherically expanding flames provided the un-stretched burning velocity of premixed CH_4- and C_3H_8-air flames with addition of CF_3Br and $C_3H_2F_3Br$. For rich flames, $C_3H_2F_3Br$ more effectively reduced the un-stretched burning velocity because, in addition to introducing halogenated radical scavengers, it shifts the overall equivalence ratio further away from stoichiometry (i.e. a fuel effect of the inhibitor). At stoichiometric conditions, the inhibitors caused a similar reduction (on a molar basis) in the burning velocity for both the CH_4- and C_3H_8-air flames. At lean conditions, CF_3Br was far more effective because $C_3H_2F_3Br$ shifts the overall mixture toward stoichiometric proportions and increased the adiabatic flame temperature by about 200 K, whereas the calculated temperature remained nearly constant with added CF_3Br.

Experiments with CH_4- and C_3H_8-air flames at equivalence ratios of 0.6, 0.8, 1.0, and 1.2 with added CF_3Br or $C_3H_2F_3Br$ at volume fractions up to $X_a = 0.04$ provided data for comparison with numerical models. Excellent agreement was observed for the CF_3Br-inhibited flames, highlighting the improved performance of the updated CF_3Br sub-model. Agreement was generally good for the $C_3H_2F_3Br$-inhibited flames at stoichiometric and rich conditions for both the CH_4- and C_3H_8-air mixtures. For lean conditions ($\Phi = 0.6$), predicted burning velocity was within 5 % to 25 % (which corresponds to a discrepancy of about 2 cm/s).

Both linear and non-linear extrapolation methods were used for determining the un-stretched laminar burning velocities S_u^0. The two approaches yielded values of S_u^0 very close to each other (i.e., within experimental error) for all conditions of the present work, except CF_3Br addition (at $X_a = 0.01$) to rich ($\Phi = 1.2$) CH_4-air flames or lean ($\Phi = 0.8$) C_3H_8-air flames (for which the linear value of S_u^0 was about 14 % and 11 % higher, respectively), and $C_3H_2F_3Br$ addition (at $X_a = 0.01$) to rich ($\Phi = 1.2$) CH_4-air flames (for which the linear value of S_u^0 was about 40 % higher).

The experiments delineated the influence of inhibitor on the flame response to stretch in terms of the burned gas Markstein length L_b. The data show that L_b is dependent on the inhibitor, fuel type, and initial equivalence ratio, with added CF_3Br or $C_3H_2F_3Br$ increasing or decreasing L_b

according to the conditions, sometimes non-monotonically. The influence of inhibitor on the flame response to stretch helped explain some conditions of non-ignition of mixtures with otherwise high enough values of S_u^0. It would be worthwhile in future research to explore the influence of ignition energy and electrode gap on the flame propagation of the present mixtures. The results have significance with regard to halogenated hydrocarbon fire suppressants and new, mildly flammable refrigerants.

ACKNOWLEDGEMENTS

The authors thank Dr. Li Qiao and Dr. Kenji Takizawa for their help during the experimental setup. We also thank Dr. Peter Sunderland at the University of Maryland and Drs. Valeri Babushok, Don Burgess, and Jeff Manion at NIST for their suggestions. This work was supported by the Boeing Company and by a NIST-ARRA grant.

REFERENCES

1. J. W. Reinhardt, D. Blake, T. Marker, Development of a minimum performance standard for aircraft cargo compartment gaseous fire suppression systems, Report No. DOT/FAA/AR-00/28, Federal Aviation Administration, Washington, D.C., USA, 2000.

2. J. W. Reinhardt, Behavior of bromotrifluoropropene and pentafluoroethane when subjected to a simulated aerosol can explosion, Report No. DOT/FAA/AR-TN04/4, Federal Aviation Administration, Washington, D.C., USA, 2004.

3. J. W. Reinhardt, Aircraft cargo MPS test of FK-5-1-12, in: International Aircraft Systems Fire Protection Working Group, October 25-26, 2006, Atlantic City, NJ, 2006, Federal Aviation Administration, Atlantic City, NJ, USA,

4. G. T. Linteris, F. Takahashi, V. R. Katta, H. K. Chelliah, O. Meier, Thermodynamic analysis of suppressant-enhanced overpressure in the FAA aerosol can simulator, in: Fire Safety Science -- Proceedings of the Tenth International Symposium, M. Spearpoint, (Ed.) College Park, MD, 6/19/2011, International Association for Fire Safety Science, Boston, MA, 2011, 307-320.

5. G. T. Linteris, D. R. Burgess, V. R. Katta, F. Takahashi, H. K. Chelliah, O. Meier, Stirred reactor calculations to understand unwanted combustion enhancement by potential halon replacements, Combust. Flame 159 (2012) 1016-1025.

6. G. T. Linteris, V. I. Babushok, P. B. Sunderland, F. Takahashi, V. R. Katta, O. Meier, Unwanted combustion enhancement by C6F12O fire suppressant, Proc. Combust. Inst. 34 (2013) 2683-2690.

7. G. T. Linteris, V. Babushok, J. L. Pagliaro, D. R. Burgess Jr, J. A. Manion, F. Takahashi, V. R. Katta, P. T. Baker, Combust. Flame, Understanding Overpressure in the FAA Aerosol Can Test by C3H2F3Br (2-BTP), accepted (2015).

8. D. R. Burgess, V. I. Babushok, G. T. Linteris, J. A. Manion, A Chemical Kinetic Mechanism for 2-Bromo-3,3,3-trifluoropropene (2-BTP) Flame Inhibition, International Journal of Chemical Kinetics 47 (2015) 533-563.

9. V. Babushok, G. T. Linteris, D. R. Burgess Jr, P. T. Baker, Hydrocarbon flame inhibition by C3H2F3Br (2-BTP), Combust. Flame 162 (2015) 1104-1112.

10. V. Babushok, T. Noto, D. R. F. Burgess, A. Hamins, W. Tsang, Influence of CF3I, CF3Br, and CF3H on the High-Temperature Combustion of Methane, Combust. Flame 107 (1996) 351-367.

11. J. L. Pagliaro, G. T. Linteris, P. B. Sunderland, P. T. Baker, Combustion inhibition and enhancement of premixed methane–air flames by halon replacements, Combust. Flame 162 (2015) 41-49.

12. L. K. Tseng, M. A. Ismail, G. M. Faeth, Laminar Burning Velocities and Markstein Numbers of Hydrocarbon/Air Flames, Combust. Flame 95 (1993) 410-426.

13. S. Kwon, L. K. Tseng, G. M. Faeth, Laminar Burning Velocities and Transition to Unstable Flames in H2/O2/N2 and C3H8/O2/N2 Mixtures, Combust. Flame 90 (1992) 230-246.

14. L. Qiao, C. Kim, G. Faeth, Suppression effects of diluents on laminar premixed hydrogen/oxygen/nitrogen flames, Combust. Flame 143 (2005) 79-96.

15. M. I. Hassan, K. T. Aung, O. C. Kwon, G. M. Faeth, Properties of laminar premixed hydrocarbon/air flames at various pressures, Journal of Propulsion and Power 14 (1998) 479-488.

16. K. Takizawa, A. Takahashi, K. Tokuhashi, S. Kondo, A. Sekiya, Burning velocity measurement of fluorinated compounds by the spherical-vessel method, Combust. Flame 141 (2005) 298-307.

17. J. E. Shephard, J. C. Krok, J. J. Lee, Spark Ignition Energy Measurements in Jet A, Report No. Explos. Dyn. Lab. Rep. FM 99e7, California Institute of Technology, Pasedena, CA, 1999.

18. A. P. Kelley, G. Jomaas, C. K. Law, Critical radius for sustained propagation of spark-ignited spherical flames, Combust. Flame 156 (2009) 1006-1013.

19. G. S. Settles, Schlieren and Shadowgraph Techniques: Visualizing Phenomena in Transparent Media., Springer, Berlin, 2001.

20. D. R. Dowdy, D. B. Smith, S. C. Taylor, A. Williams, The use of expanding spherical flames to determine burning velocities and stretch effects in hydrogen/air mixtures, Proc. Combust. Inst. 23 (1990) 325-332.

21. U. J. Pfahl, M. C. Ross, J. E. Shephard, Flammability Limits, Ignition Energy, and Flame Speeds in H2-CH4-NH3-N2O-O2-N2 Mixtures, Combust. Flame 123 (2000) 140-158.

22. L. Qiao, Y. Gu, W. J. A. Dahm, E. S. Oran, G. M. Faeth, Near-limit laminar burning velocities of microgravity premixed hydrogen flames with chemically-passive fire suppressants, Proc. Combust. Inst. 31 (2007) 2701-2709.

23. L. Qiao, Y. Gan, T. Nishiie, W. J. A. Dahm, E. S. Oran, Extinction of premixed methane/air flames in microgravity by diluents: Effects of radiation and Lewis number, Combust. Flame 157 (2010) 1446-1455.

24. Z. Chen, M. P. Burke, Y. Ju, Effects of compression and stretch on the determination of laminar flame speeds using propagating spherical flames, Combust. Theory and Modelling 13 (2009) 343-364.

25. H. Yu, W. Han, J. Santner, X. Gou, C. H. Sohn, Y. Ju, Z. Chen, Radiation-induced uncertainty in laminar flame speed measured from propagating spherical flames, Combust. Flame 161 (2014) 2815-2824.

26. Z. Chen, On the accuracy of laminar flame speeds measured from outwardly propagating spherical flames: Methane/air at normal temperature and pressure, Combust. Flame 162 (2015) 2442-2453.

27. D. Bradley, P. H. Gaskell, X. J. Gu, Burning velocities, Markstein lengths, and flame quenching for spherical methane-air flames: a computational study Combust. Flame 104 (1996) 176-198.

28. F. Halter, T. Tahtouh, C. Mounaïm-Rousselle, Nonlinear effects of stretch on the flame front propagation, Combust. Flame 157 (2010) 1825-1832.

29. Z. Chen, M. P. Burke, Y. Ju, Effects of Lewis number and ignition energy on the determination of laminar flame speed using propagating spherical flames, Proc. Combust. Inst. 32 (2009) 1253-1260.

30. A. N. Lipatnikov, S. S. Shy, W.-y. Li, Experimental assessment of various methods of determination of laminar flame speed in experiments with expanding spherical flames with positive Markstein lengths, Combustion and Flame 162 (2015) 2840-2854.

31. F. A. Williams, A review of some theoretical considerations of turbulent flame structure, in: AGARD Conference Proceeding, AGARD-CP-164, NATO Science and Technology Organization, 1975,

32. Z. Chen, On the extraction of laminar flame speed and Markstein length from outwardly propagating spherical flames, Combust. Flame 158 (2011) 291-300.

33. A. P. Kelley, C. K. Law, Nonlinear effects in the extraction of laminar flame speeds from expanding spherical flames, Combust. Flame 156 (2009) 1844-1851.

34. F. Wu, W. Liang, Z. Chen, Y. Ju, C. K. Law, Uncertainty in stretch extrapolation of laminar flame speed from expanding spherical flames, P Combust Inst 35 (2015) 663-670.

35. G. H. Markstein, Non-Steady Flame Propagation, Pergamon, New York 1964.

36. P. Clavin, Dynamic Behavior of Premixed Flame Fronts in Laminar and Turbulent Flows, Prog. in Energy and Combust. Sci. 11 (1985) 1-59.

37. N. Bouvet, F. Halter, C. Chauveau, Y. Yoon, On the effective Lewis number formulations for lean hydrogen/hydrocarbon/air mixtures, International Journal of Hydrogen Energy 38 (2013) 5949-5960.

38. P. D. Ronney, G. I. Sivashinsky, A Theoretical Study of Propagation and Extinction of Nonsteady Spherical Flame Fronts, J. Appl. Math. 49 (1989) 1029-1046.

39. A. P. Kelley, J. K. Bechtold, C. K. Law, Premixed flame propagation in a confining vessel with weak pressure rise, Journal of Fluid Mechanics 691 (2011) 26-51.

40. W. Lowry, J. de Vries, M. Krejci, E. Petersen, Z. Serinyel, W. Metcalfe, H. Curran, G. Bourque, Laminar Flame Speed Measurements and Modeling of Pure Alkanes and Alkane Blends at Elevated Pressures, Journal of Engineering for Gas Turbines and Power 133 (2011) 091501.

41. S. Gordon, McBride, B.J., Computer program for calculation of complex chemical equilibrium compositions and applications, Report No. NASA Reference Publication 1311, NASA Glenn Research Center, Cleveland, OH, 1996.

42. V. N. Huff, S. Gordon, V. E. Morrell, General method and thermodynamic tables for computation of equilibrium composition and temperature of chemical reactions, Report No. NACA-TR-1037, Cleveland, OH, USA, 1951.

43. D. R. Burgess, M. R. Zachariah, W. Tsang, P. R. Westmoreland, Thermochemical and chemical kinetic data for fluorinated hydrocarbons, Prog. Energy Combust. Sci. 21 (1995) 453-529.

44. B. N. Taylor, C. E. Kuyatt, Guidelines for Evaluating and Expressing the Uncertainty of NIST Measurement Results, Report No. NIST Technical Note 1297, National Institute of Standards and Technology, Gaithersburg, MD, 1994.

45. A. E. Lutz, F. M. Rupley, R. J. Kee, W. C. Reynolds, E. Meeks, EQUIL: A CHEMKIN implementation of STANJAN for computing chemical equilibria, S. N. Laboratories, Reaction Design, Inc., 6500 Dublin Boulevard, Dublin, CA 94568. Software and manual authorized by Ellen Meeks and Fran Rupley, 1998.

46. R. J. Kee, J. F. Grcar, M. D. Smooke, J. A. Miller, A fortran computer program for modeling steady laminar one-dimensional premixed flames, Report No. SAND85-8240, Sandia National Laboratories, Livermore, CA, USA, 1991.

47. R. J. Kee, G. Dixon-Lewis, J. Warnatz, R. E. Coltrin, J. A. Miller, A fortran computer package for the evaluation of gas-phase, multicomponent transport properties, Report No. SAND86-8246, Sandia National Laboratories, Livermore, CA, USA, 1986.

48. R. J. Kee, F. M. Rupley, J. A. Miller, CHEMKIN-II: A fortran chemical kinetics package for the analysis of gas phase chemical kinetics, Report No. SAND89-8009B, Sandia National Laboratories, Livermore, CA, USA, 1989.

49. H. Wang, X. You, K. W. Jucks, S. G. Davis, A. Laskin, F. Egolfopoulos, C. K. Law, USC Mech Version II. High-temperature combustion reaction model of H2/CO/C1-C4 compounds. <http://ignis.usc.edu/USC_Mech_II.htm> (August 2015).

50. D. Burgess, M. R. Zachariah, W. Tsang, P. R. Westmoreland, Thermochemical and Chemical Kinetic Data for Fluorinated Hydrocarbons, Report No. NIST Technical Note 1412, Gaithersburg, MD, 1995.

51. M. I. Hassan, K. T. Aung, G. M. Faeth, Measured and predicted properties of laminar premixed methane/air flames at various pressures, Combust. Flame 115 (1998) 539-550.

52. G. Rozenchan, D. L. Zhu, C. K. Law, S. D. Tse, Outward propagation, burning velocities, and chemical effects of methane flames up to 60 atm, Proc. Combust. Inst. 20 (2002) 1461-1469.

53. X. J. Gu, M. Z. Haq, M. Lawes, R. Woolley, Laminar Burning Velocity and Markstein Lengths of Methane-Air Mixtures, Combust. Flame 121 (2000) 41-58.

54. C. M. Vagelopoulos, F. N. Egolfopoulos, Direct Experimental Determination of Laminar Flame Speeds, Proc. Combust. Inst. 27 (1998) 513-519.

55. O. Park, P. S. Veloo, N. Liu, F. N. Egolfopoulos, Combustion characteristics of alternative gaseous fuels, Proc. Combust. Inst. 33 (2011) 887-894.

56. G. Jomaas, X. L. Zheng, D. L. Zhu, C. K. Law, Experimental determination of counterflow ignition temperatures and laminar flame speeds of C2–C3 hydrocarbons at atmospheric and elevated pressures, Proc. Combust. Inst. 30 (2005) 193-200.

57. F. N. Egolfopoulos, D. L. Zhu, C. K. Law, Experimental and numerical determination of laminar flame speeds: Mixtures of C2-hydrocarbons with oxygen and nitrogen, Proc. Combust. Inst. 23 (1991) 471-478.

58. K. J. Bosschaart, L. P. H. de Goey, The laminar burning velocity of flames propagating in mixtures of hydrocarbons and air measured with the heat flux method, Combust. Flame 136 (2004) 261-269.

59. E. Varea, V. Modica, A. Vandel, B. Renou, Measurement of laminar burning velocity and Markstein length relative to fresh gases using a new postprocessing procedure: Application to laminar spherical flames for methane, ethanol and isooctane/air mixtures, Combust. Flame 159 (2012) 577-590.

60. S. Balusamy, A. Cessou, B. Lecordier, Direct measurement of local instantaneous laminar burning velocity by a new PIV algorithm, Experiments in Fluids 50 (2010) 1109-1121.

61. C. Tang, Z. Huang, C. Jin, J. He, J. Wang, X. Wang, H. Miao, Laminar burning velocities and combustion characteristics of propane–hydrogen–air premixed flames, International Journal of Hydrogen Energy 33 (2008) 4906-4914.

62. E. Varea, Experimental analysis of laminar spherically expanding flames. Institut National des Sciences Appliquees de Rouen, 2013.

63. C. J. Sun, C. J. Sung, L. He, C. K. Law, Dynamics of weakly stretched flames: Qualitative description and extraction of global flame parameters, Combust Flame 118 (1999) 108-128.

64. G. Dixon-Lewis, R. J. Simpson, Aspects of flame inhibition by halogen compounds, Proc.Combust.Inst. 16 (1977) 1111-1119.

65. C. K. Westbrook, Inhibition of hydrocarbon oxidation in laminar flames and detonations by halogenated compounds, Proc. Combust. Inst. 19 (1982) 127-141.

66. D. J. Parks, N. J. Alvares, D. G. Beason, Fundamental Flame-speed Measurements in Combustion Gases Containing CF3Br, Fire Safety Journal 2 (1980) 237-247.

67. C. H. Osorio, A. J. Vissotski, E. L. Petersen, M. S. Mannan, Effect of CF3Br on C1–C3 ignition and laminar flame speed: Numerical and experimental evaluation, Combust. Flame 160 (2013) 1044-1059.

68. G. T. Linteris, L. Truett, Inhibition of premixed methane-air flames by fluoromethanes, Combust. Flame 105 (1996) 15-27.

69. G. T. Linteris, Effect of inhibitor concentration on the inhibition mechanism of fluoromethanes in premixed methane-air flames, in: A. W. Miziolek; W. Tsang, (Eds.) Halon Replacements, ACS Symposium Series 611, American Chemical Society, Washington, D.C., 1995, pp. 260-274.

70. N. Donato, C. Aul, E. Petersen, C. Zinner, H. Curran, G. Bourque, Ignition and Oxidation of 50/50 Butane Isomer Blends, J. Eng. Gas Turb. Power 132 (2010) 051502.

71. T. Noto, V. Babushok, D. R. Burgess JR., A. Hamins, W. Tsang, Effect of Halogenated Flame Inhibitors on C1-C2 Organic Flames, Twenty-Sixth Symposium on Combustion (1996) 1377-1383.

72. Z. Chen, On the extraction of laminar flame speed and Markstein length from outwardly propagating spherical flames, Combust. Flame 158 (2011) 291-300.

73. C. K. Law, Combustion physics, Cambridge University Press, 2006.

74. V. V. Zamashchikov, V. A. Alekseev, A. A. Konnov, Laminar burning velocities of rich near-limiting flames of hydrogen, International Journal of Hydrogen Energy 39 (2014) 1874-1881.

75. C. K. Law, O. C. Kwon, Effects of hydrocarbon substitution on atmospheric hydrogen–air flame propagation, International Journal of Hydrogen Energy 29 (2004) 867-879.

76. R. Sankaran, H. G. Im, Effects of Hydrogen Addition on the Markstein Length and Flammability Limit of Stretched Methane/Air Premixed Flames, Combust. Sci. Technol. 178 (2006) 1585-1611.

77. Z. Chen, Effects of hydrogen addition on the propagation of spherical methane/air flames: A computational study, International Journal of Hydrogen Energy 34 (2009) 6558-6567.

78. Z. Chen, M. P. Burke, Y. Ju, On the critical flame radius and minimum ignition energy for spherical flame initiation, Proc. Combust. Inst. 33 (2011) 1219-1226.

79. C. H. Kim, O. C. Kwon, G. M. Faeth, Effects of halons and halon replacements on hydrogen-fueled laminar premixed flames, Journal of Propulsion and Power 18 (2002) 1059-1067.